Mon. Not. R. Astron. Soc. **386,** 117–137 (2008) doi:10.1111/j.1365-2966.2008.13009.x

Spectral imaging of the Sagittarius B2 region in multiple 3-mm molecular lines with the Mopra telescope

P. A. Jones,[1⋆] M. G. Burton,[1] M. R. Cunningham,[1] K. M. Menten,[2] P. Schilke,[2] A. Belloche,[2] S. Leurini,[3] J. Ott[4,5†] and A. J. Walsh[6]

[1]*School of Physics, University of New South Wales, NSW 2052, Australia*
[2]*Max-Planck-Institut für Radioastronomie, Auf dem Hügel 69, 53121 Bonn, Germany*
[3]*European Southern Observatory, Karl-Schwarzschild-Str. 2, 85748 Garching, Germany*
[4]*National Radio Astronomy Observatory, 520 Edgemont Road, Charlottesville, VA 22903, USA*
[5]*California Institute of Technology, 1200 E. California Blvd., Pasadena, CA 91125-2400, USA*
[6]*School of Maths, Physics and IT, James Cook University, Qld 4814, Australia*

Accepted 2008 January 23. Received 2008 January 22; in original form 2007 December 3

ABSTRACT

Using the Mopra telescope, we have undertaken a 3-mm spectral-line imaging survey of a 5×5 arcmin^2 area around Sgr B2. We covered almost the complete spectral range from 81.7 to 113.5 GHz, with 2.2 MHz wide spectral channels or $\sim$6 km s^{-1} and have observed 24 lines, with 0.033 MHz wide, or $\sim$0.1 km s^{-1} channels. We discuss the distribution of around 50 lines, and present velocity-integrated emission images for 38 of the lines. In addition, we have detected around 120 more lines, mostly concentrated at the particularly spectral-line-rich Sgr B2(N) source.

There are significant differences in molecular emission, pointing to both abundance and excitation differences throughout the region. Seven distinct spatial locations are identified for the emitting species, including peaks near the prominent star-forming cores of Sgr B2(N), (M) and (S) that are seen in infrared (IR)-to-radio continuum images. The other features are a 'north ridge' and a 'north cloud' to the north of the Sgr B2 N-M-S cores, a 'south-east peak' and a 'west ridge'.

The column density, as evident through $C^{18}O$, peaks at the Sgr B2(N) and (M) cores, where strong absorption is also evident in otherwise generally bright lines such as HCO^+, HCN and HNC. Most molecules trace a ridge line to the west of the Sgr B2 N-M-S cores, wrapping around the cores and extending north-east to the north cloud. This is most clearly evident in the species HC_3N, CH_3CN, CH_3OH and OCS. They are found to be closer in distribution to the cooler dust traced by the submillimetre continuum than either the warmer dust seen in the mid-IR or to the radio continuum. The molecule CN, in contrast, is reasonably uniform over the entire region mapped, aside from strong absorption at the positions of the Sgr B2(N) and (M) cores.

Key words: ISM: individual: Sagittarius B2 – ISM: kinematics and dynamics – ISM: molecules – radio lines: ISM.

1 INTRODUCTION

Sagittarius B2 (Sgr B2) (G0.7−0.0) is a very massive and well-studied molecular cloud complex near the centre of the Galaxy. It contains multiple centres of (in many cases) spectacular star formation activity. The name derives from low-resolution radio observations where Sagittarius A is the strong source at the Galactic Centre proper (Piddington & Minnett 1951) and B1, B2, C, D and E refer to other radio and mid-infrared (mid-IR) features nearby (Lequeux 1962; Hoffmann, Frederick & Emery 1971), albeit with some confusion in the literature (Palmer & Goss 1996).

Sgr B2 is about 100 pc in projected distance from the Galactic Centre and we assume its distance from the Sun to be identical to the latter's, R_o. An R_o of 7.1 ± 1.5 kpc was measured by Reid et al. (1988) using a kinematic parallax method. A more precise distance is the 'best estimate' value of 8.0 ± 0.5 kpc that Reid (1993) derived by combining this with other data for the Galactic Centre. The latter is corroborated by the value of $R_o = 7.9 \pm 0.4$ kpc that has recently been determined from orbital solutions of a star moving around the

⋆E-mail: pjones@phys.unsw.edu.au
†Jansky Fellow of the National Radio Astronomy Observatory

supermassive central black hole, Sgr A* (Eisenhauer et al. 2003). In the following we assume $R_o = 8$ kpc.

Sgr B2 presents itself as the strongest feature in images of emission in ^{12}CO, ^{13}CO (Oka et al. 1998) and CS (Tsuboi, Handa & Ukita 1999) that define the bar-shaped (Sawada et al. 2004) central molecular zone (CMZ), which stretches over the central few hundred pc of the Galaxy. The total mass of Sgr B2 is $>5 \times 10^6\,M_\odot$ and its peak H_2 column density $\geqslant 10^{24}$ cm^{-2} (Lis & Goldsmith 1990).

Recent star formation is indicated by a giant H II region (Mehringer et al. 1993), with many compact and ultracompact H II regions (Gaume et al. 1995). There are multiple centres of maser emission from the water (McGrath, Goss & De Pree 2004), hydroxyl (Gaume & Claussen 1990) and formaldehyde (Mehringer, Goss & Palmer 1994) molecules, as well as class I and class II methanol masers (Caswell 1996; Mehringer & Menten 1997). The region's huge far-IR luminosity requires several young O-type stars as power sources, which are deeply embedded in the molecular cores.

The star-forming centres are located in a north–south line about 2 arcmin ($\sim$5 pc) long, in components labelled (north to south) Sgr B2(N), Sgr B2(M) and Sgr B2(S). All have prominent radio H II free–free, millimetre and submillimetre (Gordon et al. 1993; Pierce-Price et al. 2000) and IR (Goldsmith et al. 1992) emission. These cores have been extensively studied with millimetre spectral-line surveys (Cummins, Linke & Thaddeus 1986; Turner 1989; Nummelin et al. 1998, 2000; Belloche et al. 2005, 2007).

Sgr B2(N) is particularly rich in complex molecules: it has been called the 'Large Molecule Heimat' (Snyder, Kuan & Miao 1994; Miao et al. 1995) or LMH. Sgr B2(N) is considered to be in a more recent stage of star formation than Sgr B2(M) (Miao et al. 1995), due to the presence of the complex molecules, stronger H_2O masers, and the relatively large amount of dust.

The surrounding molecular cloud has complex kinematics. The densest core emits around 60–65 km s^{-1}, but there is a 'hole' in the CO and CS emission around 40–50 km s^{-1} in this area (Sato et al. 2000). This has been attributed (Hasegawa et al. 1994) to a collision between the 40–50 km s^{-1} cloud and a cloud at 70–80 km s^{-1}, triggering the star formation activity. There is also a cloud 2 arcmin north of Sgr B2(M), and 1 arcmin north of Sgr B2(N), with chemical enhancement in HNCO and $HOCO^+$ (Minh et al. 1998), which may be associated with the shock from this collision.

We present here a multiline spectral study in the 3-mm band, of the central 12 pc of the Sgr B2 complex, to probe the chemistry and kinematics with a wide range of molecular tracers. The data were obtained with a new 8 GHz wide spectrometer on the Mopra millimetre wave telescope in Australia. These are the initial results of a project to map the CMZ in a variety of molecular species emitting in the 3-mm band.

2 OBSERVATIONS AND DATA REDUCTION

The observations were made with the 22-m Mopra radio telescope, in on-the-fly (OTF) mapping mode (Ladd et al. 2005).

During 2005 a new wide-bandwidth digital filter bank, MOPS, was installed. This takes advantage of the wide bandwidth of the MMIC receiver, also installed in 2005, which covers the range from 77 to 117 GHz and has a wide front-end bandwidth. The MOPS can cover 8 GHz of bandwidth simultaneously, in either a broad-band mode covering the whole band in four 2.2 GHz wide spectra, or a zoom mode where several narrower spectral bands of 137 MHz can be selected within the overall 8 GHz. In both the broad-band and zoom modes, two polarizations are detected.

The observations made in 2006 June had 1024 channels in each 2.2 GHz in the broad-band mode giving channel width 2.15 MHz or around 6.4 km s^{-1} (at 100 GHz). This is coarser velocity sampling than desirable, but does allow the whole 8-GHz spectrum to be covered for a single tuning, and most of the 3-mm band in four tunings. The narrow-band mode allowed a maximum of eight zoom spectra of 137 MHz with 4096 channels (0.033 MHz or 0.10 km s^{-1} at 100 GHz) to be observed (with a maximum of four zooms in each 2.2-GHz section) or eight lines to be selected at high spectral resolution within the 8-GHz band covered by a single tuning.

This period was while the MOPS was still being upgraded, and the performance has since improved to allow up to 8192 channels of 0.27 MHz for each 2.2-GHz window in the broad-band mode and up to 16 zoom spectra simultaneously. Further observations in this Mopra CMZ mapping project in 2007 and onwards use this increased performance.[1]

The OTF observations covered an area 5×5 arcmin^2 centred on $(\alpha, \delta)_{J2000} = 17^h47^m19\overset{s}{.}8,\ -28^\circ22'17''$, i.e. close to Sagittarius B2(N). We observed this area in both the broad-band and zoom modes, in several tunings, as summarized in Table 1. The broad-band ranges are calculated assuming an overall range of 8 GHz: the data cover a bit more spectral range with 2.2-GHz subband spectra separated by 2.0 GHz, but are poor at the subband edges.

The OTF observations were made in a similar mode as for the Mopra G333−0.5/RCW106 survey (Bains et al. 2006). We used position switching for bandpass calibration with an off-source reference position $(\alpha, \delta)_{J2000} = 17^h51^m03\overset{s}{.}6,\ -28^\circ22'47''$, or $l = 1\overset{\circ}{.}093, b = -0\overset{\circ}{.}735$. observed before each 5 arcmin long source scan. The spectra were read out with 2 s of integration time. The scan lines were separated by about 10 arcsec, so around 30 scan lines were needed, taking around an hour in total. Observations of SiO maser positions were used to correct the telescope pointing, before every map, giving a pointing accuracy better than 10 arcsec. The system temperature was calibrated with a noise diode, and hot load (paddle).

The OTF data were reduced into FITS data cubes with the LIVEDATA and GRIDZILLA packages.[2] LIVEDATA is the processing software originally designed for the Parkes H I multibeam survey and is used to apply system temperature calibration, bandpass calibration, heliocentric correction, spectral smoothing and to write out the data in sdfits (Garwood 2000) format. GRIDZILLA is a regridding software package that is used to form three-dimensional (RA–Dec.–velocity) data cubes from bandpass-calibrated sdfits files (usually from LIVEDATA). The raw data files in rpfits[3] format were corrected with LIVEDATA for bandpass by the off-source spectra, a robust second order polynomial fit to the baseline subtracted and output as sdfits spectra. These were then regridded into data cubes using GRIDZILLA, with a Gaussian smoothing function for the interpolation.

The resolution of the Mopra beam varies between 36 arcsec at 86 GHz and 33 arcsec at 115 GHz (Ladd et al. 2005), so the resolution in the final data varies between 39 and 36 arcsec after convolution with the 15 arcsec full width at half-maximum (FWHM) Gaussian in the GRIDZILLA interpolation. The main beam efficiency of Mopra varies between 0.49 at 86 GHz, 0.44 at 100 GHz and 0.42 at

[1] In 2007 we have observed the frequency range 85.3–93.3 GHz in broad-band mode, over the area longitude $-0\overset{\circ}{.}2$ to $0\overset{\circ}{.}9$, and latitude $-0\overset{\circ}{.}20$ to $0\overset{\circ}{.}12$, and will discuss these observations in a later paper.

[2] http://www.atnf.csiro.au/people/mcalabre/livedata.html.

[3] http://www.atnf.csiro.au/computing/software/rpfits.html.

Table 1. Log of Mopra observations. The rms noise of the zoom bands is given for the nine-point Hanning smoothed data with 0.13-MHz channels, whereas for the broad-band data it is 2.15 MHz per channel.

Date 2006 June	Time UT (h m)	Mode	Central frequency (GHz)	Broad-band range and subband centres (GHz)	rms T_{MB} (K)
27	13 05	Broad	85.70	81.70–89.70 and 82.662, 84.734, 86.664, 88.736	0.12, 0.16, 0.11, 0.09
27	15 20	Broad	94.13	90.13–98.13 and 91.093, 93.165, 95.095, 97.167	0.14, 0.16, 0.13, 0.17
27	16 26	Broad	102.78	98.78–106.78 and 99.742, 101.814, 103.744, 105.816	0.21, 0.33, 0.23, 0.18
28	09 19	Broad	109.48	105.48–113.48 and 106.452, 108.524, 110.454, 112.526	0.15, 0.17, 0.24, 0.35
27	11 51	Zoom	85.70	85.146, 85.560, 86.112, 86.802, 87.354, 87.906, 88.596, 89.148	0.22–0.29
29	12 09	Zoom	94.13	90.678, 90.954, 91.920, 93.162, 94.404, 96.750, 97.302, 97.992	0.26–0.38
27	17 50	Zoom	102.78	99.328, 100.018, 100.570, 101.536, 102.088, 102.502, 103.054, 104.572	0.32–0.42

115 GHz (Ladd et al. 2005). These parameters were measured however by Ladd et al. (2005) with a previous receiver and correlator. Since we are more concerned in this paper with the spatial and velocity structure, we have left the intensities throughout in this paper in the T_A^* scale, without correction for the beam efficiency on to the T_{MB} scale (except for the rms noise in Table 1).

The zoom mode data, with high resolution in velocity, were output as cubes over the velocity range -30 to 170 km s^{-1}, to reduce the file size, using the appropriate rest frequency of the line targeted. The broad-band mode cubes were made with frequency as the third axis, over the whole 1024 channels of each subband. The pixel size was 12 arcsec. The FITS cubes were then read into the MIRIAD package for further analysis.

The integrated spectra over the region were plotted for the broad-band mode data cubes, to identify the lines detected. Because of ripples in the spectra, particularly at the bandpass edges (mostly correlator ringing or 30-MHz ripples due to standing waves between the main dish and the secondary), we did not always reach the expected thermal noise sensitivity of around $T_{MB} = 0.1$ K (see Table 1). However, we identified several dozen strong lines (see Table 2) in the average spectra over the broad-band data cubes. These lines were identified using the NIST online data base (Lovas 2002). For these lines we extracted subregions of 100 channels (~ 650 km s^{-1}) from the frequency cubes, and relabelled the scale as velocity, by putting the appropriate rest frequency into the file headers. These made low velocity resolution data cubes for the broad-band mode data.

Since the lines are broad compared to the 0.033-MHz frequency channels of the zoom mode data, we also made smoothed versions of the zoom mode cubes, with a nine-point Hanning function, to improve the signal-to-noise ratio of the spectra, and using every fourth channel to reduce the file size, making 0.13-MHz channels.

For both the zoom mode and broad-band mode data cubes, we then made integrated emission images, by summing the data over velocity, using velocity range over which the emission was well above the noise level. This velocity range differed depending on whether the particular line had strong line wings. These images are plotted and discussed in Section 3.

In addition, we searched the broad-band data cubes, visually plane by plane, to identify line emission which was weak or not very extended, and so was not obvious in the spectrum integrated over the whole area. There are around 120 of these additional lines, which are listed in Table 3. Most of these are known lines, in the NIST online data base (Lovas 2002). The line around 107.63 GHz is attributed to multiple blended transitions of CH_3CH_2CN $v = 1$ (John Pearson, private communication).

The additional lines (Table 3) are discussed below, in Section 3, but as the line emission is weak and noisy, and mostly confined to a small area, the images are not plotted here.

The mapped area of 5 arcmin corresponds to 12 pc, and the resolution is 1.4–1.5 pc (using the Galactic Centre distance $R_o = 8.0$ kpc).

3 RESULTS

We present here the integrated emission images, analysis of these images and the data cubes. An area of 5.2×5.2 arcmin^2 is plotted for each image, generally using the same right ascension (RA) and declination (Dec.) scale for the axes, to allow easy comparison. Images from the broad-band 109-GHz tuning cover a region with slight offset in RA to the other images, as these data had a small ($\sim$24 arcsec) systematic shift in position, which has been corrected. (The origin of this offset is not clear, but is probably due to a poor pointing correction made just before these data were collected.) Integrated emission images use the mean of broad-band and zoom mode, if the zoom mode data were available (or we use the better image if one of the broad or zoom data had problems). The OTF scanning direction was in RA, and some of the images show stripe artefacts in this direction.

We plot positions of radio sources with crosses, to make the alignment of different features more obvious. The radio positions are taken from the 9.1 GHz continuum peaks of Hunt et al. (1999) obtained with the Australia Telescope Compact Array, supplemented by a few positions of peaks from 20-cm Very Large Array (VLA) data for sources outside the area of Hunt et al. (1999). Note in particular that the peak near the centre is Sgr B2(N) at J2000 17 47 20.4, -28 22 12, with Sgr B2(M) at 17 47 20.5, -28 23 05 and Sgr B2(S) at 17 47 20.5, -28 23 44 in a line almost exactly to the south (labelled in Fig. 1). We also plot with open squares, some mid-IR sources with positions fitted from the 21-μm (band E) *Midcourse Space Experiment* (*MSX*) data (Price et al. 2001). Note that the four mid-IR peaks all correspond to radio sources, including Sgr B2(M) and Sgr B2(S) but that Sgr B2(N) does not have strong emission at 21 μm. See Section 4 for plots of the radio and mid IR continuum, and discussion of the alignment of the different molecular lines with the radio and mid-IR continuum features.

In the figure captions we give peak integrated brightness and contour level steps, in K km s^{-1}, on the T_A^* scale, that is not corrected for beam efficiency. The contours are in equal linear steps. In most cases the lowest contour level is the same as the step size, but this is not the case for some of the strongest lines (such as ^{12}CO) where

Table 2. Summary of strong lines detected from the broad-band mode observations. The flag Z in the last column indicates lines for which there is zoom mode data with higher velocity resolution. For most of these lines we show integrated images in Figs 1, 3–7 and 9.

Rough frequency (GHz)	Line ID molecule	Transition	Exact rest frequency (GHz)	
81.88	HC_3N	9–8	81.881 462	
84.52	CH_3OH	5(−1,5)–4(0,4) E	84.521 206	
85.14	OCS	7–6	85.139 104	Z
85.27	CH_3CH_2OH	6(0,6)–5(1,5)	85.265 507	
85.34	c-C_3H_2	2(1,2)–1(0,1)	85.338 906	
85.46	CH_3CCH	5(3)–4(3)	85.442 600	
		5(2)–4(2)	85.450 765	
		5(1)–4(1)	85.455 665	
		5(0)–4(0)	85.457 299	
85.53	$HOCO^+$	4(0,4)–3(0,3)	85.531 480	Z
86.09	SO	2(2)–1(1)	86.093 983	Z
86.34	$H^{13}CN$	1–0 F = 1–1	86.338 735	
		1–0 F = 2–1	86.340 167	
		1–0 F = 0–1	86.342 256	
86.75	$H^{13}CO^+$	1–0	86.754 330	
86.85	SiO	2–1 $v = 0$	86.847 010	Z
87.09	$HN^{13}C$	1–0 F = 0–1	87.090 735	
		1–0 F = 2–1	87.090 859	
		1–0 F = 1–1	87.090 942	
87.32	C_2H	1–0 3/2–1/2 F = 2–1	87.316 925	Z
		1–0 3/2–1/2 F = 1–0	87.328 624	
87.40	C_2H	1–0 −1–1/2 F = 1–1	87.402 004	Z
		1–0 −1–1/2 F = 0–1	87.407 165	
87.93	HNCO	4(0,4)–3(0,3)	87.925 238	Z
88.63	HCN	1–0 F = 1–1	88.630 4157	Z
		1–0 F = 2–1	88.631 8473	
		1–0 F = 0–1	88.633 9360	
89.19	HCO^+	1–0	89.188 526	Z
90.66	HNC	1–0 F = 0–1	90.663 450	Z
		1–0 F = 2–1	90.663 574	
		1–0 F = 1–1	90.663 656	
90.98	HC_3N	10–9	90.978 989	Z
91.99	CH_3CN	5(3)–4(3) F = 6–5	91.971 310	Z
		5(3)–4(3) F = 4–3	91.971 465	
		5(2)–4(2) F = 6–5	91.980 089	
		5(1)–4(1)	91.985 316	
		5(0)–4(0)	91.987 089	
92.49	^{13}CS	2–1	92.494 303	
93.17	N_2H^+	1–0 F_1 = 1–1 F = 0–1	93.171 621	Z
		1–0 F_1 = 1–1 F = 2–2	93.171 917	
		1–0 F_1 = 1–1 F = 1–0	93.172 053	
		1–0 F_1 = 2–1 F = 2–1	93.173 480	
		1–0 F_1 = 2–1 F = 3–2	93.173 777	
		1–0 F_1 = 2–1 F = 1–1	93.173 967	
		1–0 F_1 = 0–1 F = 1–2	93.176 265	
94.41	$^{13}CH_3OH$	2(−1,2)–1(−1,1) E	94.405 223	Z
		2(0,2)–1(0,1) A+	94.407 129	
		2(0,2)–1(0,1) E	94.410 895	
		2(1,1)–1(1,0) E	94.420 439	
95.17	CH_3OH	8(0,8)–7(1,7) A+	95.169 516	
95.91	CH_3OH	2(1,2)–1(1,1) A+	95.914 310	
96.41	$C^{34}S$	2–1	96.412 961	
96.74	CH_3OH	2(−1,2)–1(−1,1) E	96.739 393	Z
		2(0,2)–1(0,1) A+	96.741 377	
		2(0,2)–1(0,1) E	96.744 549	
		2(1,1)–1(1,0) E	96.755 507	
97.30	OCS	8–7	97.301 209	Z
97.58	CH_3OH	2(1,1)–1(1,0) A−	97.582 808	
97.98	CS	2–1	97.980 953	Z
99.30	SO	3(2)–2(1)	99.299 905	Z
100.08	HC_3N	11–10	100.076 385	Z
100.63	NH_2CN	5(1,4)–4(1,3)	100.629 50	Z
101.48	H_2CS	3(1,3)–2(1,2)	101.477 764	
102.07	NH_2CHO	5(1,5)–4(1,4)	102.064 263	Z
	H_2COH^+	4(0,4)–3(1,3)	102.065 856	
102.55	CH_3CCH	6(3)–5(3)	102.530 346	Z
		6(2)–5(2)	102.540 143	
		6(1)–5(1)	102.546 023	
		6(0)–5(0)	102.547 983	
103.04	H_2CS	3(0,3)–2(0,2)	103.040 416	Z
104.03	SO_2	3(1,3)–2(0,2)	104.029 410	
104.62	H_2CS	3(1,2)–2(1,1)	104.616 988	Z
105.79	CH_2NH	4(0,4)–3(1,3)	105.794 057	
106.91	$HOCO^+$	5(0,5)–4(0,4)	106.913 524	
108.89	CH_3OH	0(0,0)–1(−1,1) E	108.893 929	
109.17	HC_3N	12–11	109.173 638	
109.25	SO	2(3)–1(2)	109.252 212	
109.46	OCS	9–8	109.463 063	
109.78	$C^{18}O$	1–0	109.782 173	
109.91	HNCO	5(0,5)–4(0,4)	109.905 753	
110.20	^{13}CO	1–0	110.201 353	
110.38	CH_3CN	6(3)–5(3) F = 7–6	110.364 469	
		6(3)–5(3) F = 5–4	110.364 524	
		6(2)–5(2) F = 7–6	110.375 052	
		6(1)–5(1) F = 7–6	110.381 404	
		6(0)–5(0) F = 7–6	110.383 522	
112.36	$C^{17}O$	1–0	112.358 988	
113.17	CN	1–0 1/2–1/2 F = 1/2–3/2	113.144 192	
		1–0 1/2–1/2 F = 3/2–1/2	113.170 528	
		1–0 1/2–1/2 F = 3/2–3/2	113.191 317	
113.49	CN	1–0 3/2–1/2 F = 3/2–1/2	113.488 140	
		1–0 3/2–1/2 F = 5/2–3/2	113.490 982	
		1–0 3/2–1/2 F = 1/2–1/2	113.499 639	
		1–0 3/2–1/2 F = 3/2–3/2	113.508 944	

the whole 5-arcmin^2 area is filled with emission well above the zero level.

In this section we present maps for many of the lines measured. We summarize these line maps in Table 2, whereas in Table 3 we list all the other (weaker) lines detected, for which we do not present maps. We also discuss the velocities and linewidths at the emission peaks for the various maps presented. These are summarized in Table 4. We use the rough frequency in GHz, rounded to two decimal places, in the figures, Tables 2 and 3 and text below, as a convenient shorthand to refer to the lines.

3.1 ^{13}CO, C^{18}O and C^{17}O

The isotopic carbon monoxide ^{13}CO 1–0 (110.20 GHz) and C^{18}O 1–0 (109.78 GHz) integrated emission is shown in Fig. 1. The ^{13}CO emission is optically thick in the densest regions, with the ratio of the peak integrated emission of ^{13}CO/C^{18}O of around 5, rather than ∼9 for optically thin emission near the Galactic Centre (Lis & Goldsmith 1989). The dense peaks are therefore better traced by C^{18}O, which shows two peaks associated with Sgr B2(M) and Sgr B2(N), with fitted positions (J2000) 17 47 20.3, −28 23 06 and 17 47 19.5, −28 22 15, LSR velocities 63 and 68 km s^{-1} and FWHM 21 and 22 km s^{-1}, respectively.

Table 3. Summary of weaker lines detected from the broad-band mode observations. We do not show the integrated images for these lines here. The flags in the last column indicate the spatial distribution of the line: N = peak at Sgr B2(N); M = peak at Sgr B2(M); B = peaks at both Sgr B2(N) and Sgr B2(M); E = extended. Lines marked as 'Unidentified' in column 2, have been noted in previous surveys and included in the NIST data base (Lovas 2002) with the rest frequency in column 4. Lines marked as 'U' in column 2 are not in the NIST data base. These rest frequencies are quoted to the nearest MHz assuming radial velocity around 61 km s^{-1} appropriate for Sgr B2(N) and Sgr B2(M), Section 4.

Rough frequency (GHz)	Line ID molecule	Transition	Exact Rest frequency (GHz)	
82.46	CH_3OCH_3	11(1,10)–11(0,11) AE + EA	82.456 986	N
	CH_3CH_2CN	9(1,8)–8(1,7)	82.458 611	
	CH_3OCH_3	11(1,10)–11(0,11) EE	82.458 660	
	CH_3OCH_3	11(1,10)–11(0,11) AA	82.460 334	
83.69	SO_2	8(1,7)–8(0,8)	83.688 086	M
85.09	NH_2CHO	4(2,2)–3(2,1)	85.093 268	N
85.69	U		85.686	B
87.85	NH_2CHO	4(1,3)–3(1,2)	87.848 871	E
88.17	$H^{13}CCCN$	10–9	88.166 808	N
88.24	HNCO	4(1,3)–3(1,2)	88.239 027	N
89.32	CH_3OCHO	8(1,8)–7(1,7) E	89.314 589	N
	CH_3OCHO	8(1,8)–7(1,7) A	89.316 668	
89.57	CH_3CH_2CN	10(6)–9(6)	89.562 318	N
	CH_3CH_2CN	10(7)–9(7)	89.565 034	
	CH_3CH_2CN	10(5)–9(5)	89.568 100	
	CH_3CH_2CN	10(8)–9(8)	89.573 057	
89.59	CH_3CH_2CN	10(4,7)–9(4,6)	89.590 033	N
	CH_3CH_2CN	10(4,6)–9(4,5)	89.591 017	
90.45	CH_3CH_2CN	10(2,8)–9(2,7)	90.453 354	N
90.60	$HC^{13}CCN$	10–9	90.593 059	E
	$HCC^{13}CN$	10–9	90.601 791	
91.20	HC_3N	10–9 $v_6 = 1\, l = 1$ f	91.199 796	N
	HC_3N	10–9 $v_7 = l\, l = 1$ e	91.202 607	
91.33	HC_3N	10–9 $v_7 = 1\, l = 1$ f	91.333 308	N
91.55	CH_3CH_2CN	10(1,9)–9(1,8)	91.549 117	N
	SO_2	18(5,13)–19(4,16)	91.550 442	
91.60	Unidentified		91.603	N
91.84	Unidentified		91.848	N
92.04	U		92.035	M
92.26	CH_3CN	5(0)–4(0) $v_8 = 1\, l = 1$	92.261 440	N
	CH_3CN	5(2)–4(2) $v_8 = 1\, l = 1$	92.263 992	
92.43	CH_2CHCN	10(1,10)–9(1,9)	92.426 260	N
93.60	CH_3CHO	5(−1,5)–4(−1,4) E	93.595 238	E
93.87	CCS	8(7)–7(6)	93.870 098	E
	NH_2CHO	3(2,2)–4(1,3)	93.871 700	
94.28	CH_2CHCN	10(0,10)–9(0,9)	94.276 640	N
94.54	CH_3OH	8(3,5)–9(2,7) E	94.541 806	N
94.76	U		94.759	N
94.91	CH_2CHCN	10(4,7)–9(4,6)	94.913 139	N
	CH_2CHCN	10(4,6)–9(4,5)	94.913 250	
94.92	U		94.924	N
94.94	U		94.940	N
95.15	Unidentified		95.145	E
95.33	CH_2CHCN	10(2,8)–9(2,7)	95.325 490	N
95.44	CH_3CH_2CN	11(1,11)–10(1,10)	95.442 479	N
	t-CH_3CH_2OH	16(2,14)–16(1,13)	95.444 067	
95.95	CH_3CHO	5(0,5)–4(0,4) E	95.947 439	E
95.96	CH_3CHO	5(0,5)–4(0,4) A++	95.963 465	E
96.49	CH_3OH	2(1,2)–1(1,1) E $v_t = 1$	96.492 164	N
	CH_3OH	2(0,2)–1(0,1) E $v_t = 1$	96.493 553	
96.98	$O^{13}CS$	8–7	96.988 123	E
97.70	SO_2	7(3,5)–8(2,6)	97.702 340	M
97.72	^{34}SO	3(2)–2(1)	97.715 401	M
98.18	CH_3CH_2CN	11(2,10)–10(2,9)	98.177 578	N
	CH_3OCHO	8(7,1)–7(7,0) E	98.182 199	
98.90	CH_3CHO	5(1,4)–4(1,3) A−	98.900 951	E
99.02	U		99.021	M
99.65	$HC^{13}CCN$	11–10	99.651 863	N
	$HCC^{13}CN$	11–10	99.661 471	
99.68	CH_3CH_2CN	11(2,9)–10(2,8)	99.681 511	N
100.03	SO	4(5)–4(4)	100.029 565	B
100.32	HC_3N	11–10 $v_7 = 1\, l = 1$ e	100.322 349	N
100.41	U		100.406	M
100.46	CH_3OCH_3	6(2,5)–6(1,6) EA + AE	100.460 412	N
	CH_3OCH_3	6(2,5)–6(1,6) EE	100.463 066	
	CH_3OCH_3	6(2,5)–6(1,6) AA	100.465 708	
100.61	CH_3CH_2CN	11(1,10)–10(1,9)	100.614 291	N
100.71	HC_3N	11–10 $v_7 = 2\, l = 0$	100.708 837	N
	HC_3N	11–10 $v_7 = 2\, l = 2$ e	100.710 972	
	HC_3N	11–10 $v_7 = 2\, l = 2$ f	100.714 306	
100.88	SO_2	2(2,0)–3(1,3)	100.878 105	M
101.03	CH_2CO	5(2,4)–4(2,3)	101.024 438	N
	CH_3SH	4(−1)–3(−1) E	101.029 750	
101.14	CH_3SH	4(0)–3(0) A	101.139 160	E
	CH_3SH	4(0)–3(0) E	101.139 650	
101.33	H_2CO	6(1,5)–6(1,6)	101.332 987	N
101.98	CH_2CO	5(1,4)–4(1,3)	101.981 426	E
103.57	CH_2CHCN	11(0,11)–10(0,10)	103.575 401	N
104.05	CH_3CH_2CN	12(1,12)–11(1,11)	104.051 278	N
104.21	CH_2CHCN	11(2,10)–10(2,9)	104.212 655	N
104.24	SO_2	10(1,9)–10(0,10)	104.239 293	B
104.30	CH_3OH	11(−1,11)–10(−2,9) E	104.300 396	N
104.35	CH_3OH	10(4,7)–11(3,8) A−	104.354 861	N
104.41	CH_2CHCN	11(5,*)–10(5,*)	104.408 903	N
	CH_3OH	10(4,6)–11(3,9) A+	104.410 489	
	CH_2CHCN	11(4,8)–10(4,7)	104.411 262	
	CH_2CHCN	11(4,7)–10(4,6)	104.411 485	
104.49	*t*-CH_3CH_2OH	7(0,7)–6(1,6)	104.487 254	E
104.80	*t*-CH_3CH_2OH	5(1,5)–4(0,4)	104.808 618	E
104.96	CH_2CHCN	11(2,9)–10(2,8)	104.960 550	N
105.06	CH_3OH	13(1,13)–12(2,10) A+	105.063 761	N
105.30	U		105.299	M
105.46	NH_2CHO	5(0,5)–4(0,4)	105.464 216	E
	CH_3CH_2CN	12(0,12)–11(0,11)	105.469 300	
105.54	U		105.537	N
105.57	CH_3OH	14(-2,13)–14(1,13) E	105.576 385	N
105.77	CH_3OCH_3	13(1,12)–13(0,13) EA + AE	105.768 276	N
	CH_3OCH_3	13(1,12)–13(0,13) EE	105.770 340	
	CH_3OCH_3	13(1,12)–13(0,13) AA	105.772 403	

Table 3 – *continued*

Table 3 – *continued*

Rough frequency (GHz)	Line ID molecule	Transition	Exact Rest frequency (GHz)	
105.97	NH_2CHO	5(2,4)–4(2,3)	105.972 593	N
106.11	U		106.107	N
106.13	NH_2CHO	5(3,3)–4(3,2)	106.134 418	B
106.35	CCS	9(8)–8(7)	106.347 740	E
106.54	NH_2CHO	5(2,3)–4(2,2)	106.541 674	N
106.64	CH_2CHCN	11(1,10)–10(1,9)	106.641 394	N
106.74	^{34}SO	2(3)–1(2)	106.743 374	M
107.01	CH_3OH	3(1,3)–4(0,4) A+	107.013 770	B
107.04	U		107.042	N
107.06	SO_2	27(3,25)–26(4,22)	107.060 225	M
107.10	Unidentified		107.1032	E
107.16	CH_3OH	15(−2,14)–15(1,14) E	107.159 915	N
107.19	$^{13}CH_3CN$	6(1)–5(1)	107.194 547	N
	$^{13}CH_3CN$	6(0)–5(0)	107.196 564	
107.48	CH_3CH_2CN	17(2,16)–17(1,17)	107.481 465	N
	CH_3CH_2CN	12(7,*)–11(7,*)	107.485 181	
	CH_3CH_2CN	12(6,*)–11(6,*)	107.486 962	
	CH_3CH_2CN	12(8,*)–11(8,*)	107.491 579	
107.50	CH_3CH_2CN	12(5,8)–11(5,7)	107.502 426	N
	CH_3CH_2CN	12(5,7)–11(5,6)	107.502 473	
107.54	CH_3CH_2CN	12(11,*)–11(11,*)	107.539 857	N
	CH_3OCHO	9(2,8)–8(2,7) A	107.543 746	
	CH_3CH_2CN	12(4,9)–11(4,8)	107.543 924	
	CH_3CH_2CN	12(4,8)–11(4,7)	107.547 599	
107.59	CH_3CH_2CN	12(3,10)–11(3,9)	107.594 046	N
107.63	CH_3CH_2CN	$v = 1$, multiple	107.636	N
107.73	CH_3CH_2CN	12(3,9)–11(3,8)	107.734 738	N
107.84	SO_2	12(4,8)–13(3,11)	107.843 478	M
108.65	^{13}CN	1/2–1/2 F = 2–1, $F_1 = 0,\ F_2 = 1$–0	108.651 297	E
	^{13}CN	1/2–1/2 F = 2–2, $F_1 = 0,\ F_2 = 1$–1	108.657 646	
	^{13}CN	1/2–1/2 F = 1–2, $F_1 = 1,\ F_2 = 1$–1	108.658 948	
108.71	$HC^{13}CCN$	12–11	108.710 523	N
	$HCC^{13}CN$	12–11	108.721 008	
108.78	^{13}CN	3/2–1/2 F = 3–2, $F_1 = 1,\ F_2 = 2$–1	108.780 201	E
	^{13}CN	3/2–1/2 F = 2–1 $F_1 = 1,\ F_2 = 2$–1	108.782 374	
	^{13}CN	3/2–1/2 F = 1–0 $F_1 = 1,\ F_2 = 2$–1	108.786 982	
108.94	CH_3CH_2CN	12(2,10)–11(2,9)	108.940 596	N
109.14	CH_3OH	26(0,26)–26(-1,26) E	109.137 570	N
109.15	CH_3OH	16(-2,15)–16(1,15) E	109.153 210	N
109.44	HC_3N	12–11 $v_6 = 1\ l = 1$ f	109.438 572	N
	HC_3N	12–11 $v_7 = 1\ l = 1$ e	109.441 944	
109.49	HNCO	5(1,5)–4(1,4)	109.496 007	E
109.60	HC_3N	12–11 $v_7 = 1\ l = 1$ f	109.598 751	B
109.65	CH_3CH_2CN	12(1,11)–11(1,10)	109.650 301	N
109.75	NH_2CHO	5(1,4)–4(1,3)	109.753 499	E
	SO_2	17(5,13)–18(4,14)	109.757 587	
109.87	HC_3N	12–11 $v_7 = 2\ l = 2$ f	109.870 188	B
	HNCO	5(1,5)–4(1,4) $v_6 = 1$	109.870 278	
	HNCO	5(2,4)–4(2,3)	109.872 366	
	HNCO	5(2,3)–4(2,2)	109.872 773	
110.29	HNCO	5(1,4)–4(1,3)	110.298 098	E
110.33	$CH_3^{13}CN$	6(2)–5(2)	110.320 438	N

Table 3 – *continued*

Rough frequency (GHz)	Line ID molecule	Transition	Exact Rest frequency (GHz)	
	$CH_3^{13}CN$	6(1)–5(1)	110.326 795	
	$CH_3^{13}CN$	6(0)–5(0)	110.328 914	
	CH_3CN	6(5)–5(5) F = 7–6	110.330 627	
	CH_3CN	6(5)–5(5) F = 5–4	110.330 872	
110.35	CH_3CN	6(4)–5(4) F = 7–6	110.349 659	E
	CH_3CN	6(4)–5(4) F = 5–4	110.349 797	
110.69	CH_3CN	6(2)–5(2) $v_8 = 1$ $l = -1$	110.695 506	N
	CH_3CN	6(4)–5(4) $v_8 = 1$ $l = 1$	110.698 701	
110.71	CH_3CN	6(1)–5(1) $v_8 = 1$ $l = -1$	110.706 251	N
	CH_3CN	6(3)–5(3) $v_8 = 1$ $l = +1$	110.709 313	
	CH_3CN	6(0)–5(0) $v_8 = 1$ $l = 1$	110.712 166	
	CH_3CN	6(2)–5(2) $v_8 = 1$ $l = 1$	110.716 212	
111.29	CH_3OH	7(2,5)–8(1,8) A+	111.289 601	N
112.64	CH_3CH_2CN	13(1,13)–12(1,12)	112.646 233	N
112.84	U		112.839	N
113.12	CN	1–0 $J = 1/2$–$1/2$ F = 1/2–1/2	113.123 337	E

The ^{13}CO data cube, with intensity as a function of velocity (Fig. 2), agrees well with the results of Sato et al. (2000) and Hasegawa et al. (2008), showing the low-velocity 'hole' at 40–50 km s^{-1} and the high-velocity 'clump' at 70–80 km s^{-1}. However, the broad-band data here are with poorer velocity and spatial resolution than that of Sato et al. (2000) or Hasegawa et al. (2008), so we do not resolve details in the spatial and velocity structure that they attribute to their cloud–cloud collision model (Hasegawa et al. 1994). The integrated ^{13}CO and $C^{18}O$ images (Fig. 1) also show the northern emission ridge or 'edge' (Hasegawa et al. 1994) with peak at 17 47 24.2, −28 20 49 (in ^{13}CO) with central velocity 65 km s^{-1} (width 42 km s^{-1}) from ^{13}CO and 63 km s^{-1} (width 36 km s^{-1}) from $C^{18}O$. There is also the higher velocity ridge to the west in ^{13}CO (Fig. 2) with peak at 17 47 14.0 −28 22 14, velocity 109 km s^{-1} (width 32 km s^{-1}).

We have also imaged the weaker $C^{17}O$ 1–0 (112.36 GHz) data, which shows the densest CO peak near Sgr B2(M) at around 64 km s^{-1}. However, the $C^{17}O$ data are affected by the bandpass ripples, so we do not show the integrated image here, or consider further quantitative analysis (such as line ratios).

3.2 CS, ^{13}CS and C^{34}S

The carbon monosulphide CS 2–1 (97.98 GHz) integrated emission is shown in Fig. 3. The CS data cube (not shown here) shows that the main peak near Sgr B2(M) has a minimum around velocity 62 km s^{-1}, due to self-absorption at the position and velocity where the brightest CO is found. The CS also traces the low-velocity 'hole' at $\sim$ 35 km s^{-1} similar to the results of Sato et al. (2000) and Tsuboi et al. (1999) using the CS 1–0 line at 48.99 GHz.

The CS 2–1 emission near Sgr B2(M) shows a velocity gradient, with the emission wings on either side of the 62 km s^{-1} self-absorption offset: the peak around 85 km s^{-1} is at 17 47 19.8,

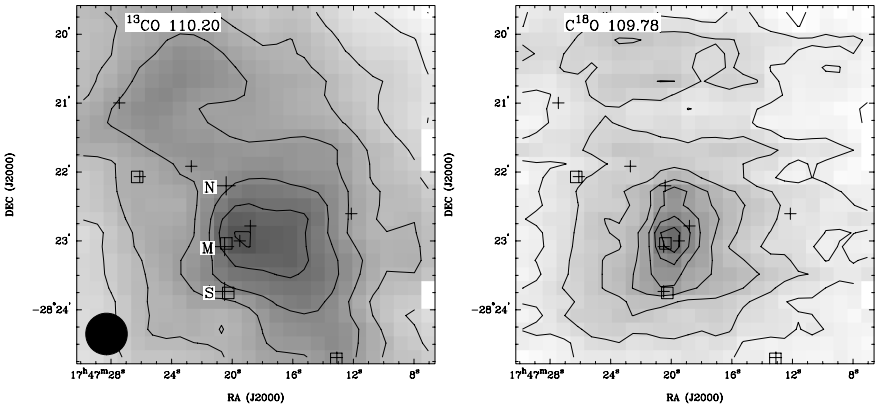

Figure 1. Integrated emission for ^{13}CO and C^{18}O. In this, and subsequent images, the crosses indicate positions of radio peaks, as described in Section 3, including in particular the positions of Sgr B2(N), (M) and (S). The squares show mid-IR sources. The optically thin C^{18}O peaks near Sgr B2(M), while the ^{13}CO shows the widespread diffuse emission. The peak brightness and contour steps are 240 and 20 K km s^{-1} for ^{13}CO, and 48 and 5 K km s^{-1} for C^{18}O. The beam size is shown in the bottom left-hand corner of the ^{13}CO image.

−28 22 56 and the peak around 50 km s^{-1} is at 17 47 19.5, −28 23 06. This is shown at higher resolution in BIMA observations of Mehringer (1995) who attribute this to an outflow. The blueshifted wing is stronger, so that the integrated CS emission peaks at around 17 47 19.2, −28 23 03 to the south-west of Sgr B2(M). There is very little CS emission from Sgr B2(N) indicating that it is underabundant in CS, relative to Sgr B2(M).

The CS data cube also shows the 'south-east CS peak' noted by Yusef-Zadeh et al. (1996), centred at 17 47 27.1, −28 23 13, at 41 km s^{-1}, width 20 km s^{-1}; the north ridge with peak at 17 47 22.3, −28 20 49, at 61 km s^{-1}, width 57 km s^{-1}; and the west ridge with peak at 17 47 14.9, −28 22 37, at 119 km s^{-1}, width 14 km s^{-1} (Sato et al. 2000).

We also have data (not plotted here) from ^{13}CS 2–1 (92.49 GHz) and C^{34}S 2–1 (96.41 GHz) transitions, which are much weaker, but are optically thin and do not suffer as much from the self-absorption. These confirm the lower CS emission from Sgr B2(N) than from Sgr B2(M), and show that the peak near Sgr B2(M) is at 17 47 18.7, −28 23 11 with velocity around 54 km s^{-1}, width 15 km s^{-1}.

3.3 HCO$^+$, HCN, HNC, H^{13}CO$^+$, H^{13}CN and HN^{13}C

The integrated emission distributions of formylium HCO$^+$ 1–0 (89.19 GHz), hydrogen cyanide HCN 1–0 (88.63 GHz) and hydrogen isocyanide HNC 1–0 (90.66 GHz) are shown in Fig. 3. The distributions are qualitatively similar, but require careful interpretation as they are strongly affected by self-absorption. In particular, the low level of integrated emission in the centre, near Sgr B2(N) and Sgr B2(M), is due to absorption, as is shown, for example, in the spectra and integrated images of Jacq et al. (1999).

The whole area is filled with emission over a wide velocity range. Fitting spectra at the east edge of the imaged area, away from the strong absorption in the centre, we find a peak velocity of 70 km s^{-1}, width 71 km s^{-1} for HCO$^+$, velocity 69 km s^{-1}, width 77 km s^{-1} for HCN and velocity 55 km s^{-1}, width 67 km s^{-1} for HNC. This component is enhanced in the area of the north ridge in HNC, with peak position 17 47 22.0, −28 20 55, and single-component fit velocity 59 km s^{-1}, width 54 km s^{-1} (but there is some self-absorption at this position, making the single-component Gaussian not a very good fit). The west ridge adds to this wide component, in the integrated images (Fig. 3), but is not well separated in velocity. Multicomponent fits to the spectra show that it peaks at 17 47 14.8 −28 22 36 in HCO$^+$ (we cannot get a good fit to this component in velocity), peak 17 47 14.7 −28 22 34, velocity 119 km s^{-1}, width 24 km s^{-1} in HCN and peak 17 47 14.9 −28 22 34, velocity 112 km s^{-1}, width 21 km s^{-1} in HNC.

The HCO$^+$, HCN and HNC data cubes show a peak near Sgr B2(M), much like that in CS, with self-absorption around 65 km s^{-1}. The spectra from this area show two components around 46 and 90 km s^{-1}, which are interpreted as a single component with an absorption dip. There is also absorption of the Sgr B2 continuum emission, by gas along the line of sight, giving a broad negative feature to the spectra between velocities −120 and 20 km s^{-1}. Quantitative analysis of the peak near Sgr B2(M) is affected by the absorption.

The fitted peak positions (at around 90 km s^{-1}) are 17 47 20.1, −28 22 34 in HCO$^+$, 17 47 20.1, −28 22 32 in HCN and 17 47 19.8, −28 22 56 in HNC. This is near the CS peak and the C^{18}O peak, but as for CS, there may be a gradient of position with velocity. We also have data (not plotted here) of the corresponding weaker isotopologue lines H^{13}CO$^+$ 1–0 (86.75 GHz), H^{13}CN 1–0 (86.34 GHz) and HN^{13}C 1–0 (87.09 GHz) which also show some self-absorption, but are less affected, and hence better for the velocity fits. The velocities are peak 50 km s^{-1}, width 8 km s^{-1} for H^{13}CO$^+$, peak 47 km s^{-1}, width 12 km s^{-1} for H^{13}CN and peak 52 km s^{-1}, width 16 km s^{-1} for HN^{13}C. The HN^{13}C fit is in good agreement with the fit to the CS peak but the other two are a bit lower in velocity and narrower, presumably due to the effect of the absorption.

Note that the HCN, HNC, H^{13}CN and HN^{13}C lines are triplets with hyperfine splitting, but that the spread of frequency for HNC and HN^{13}C is only 0.21 MHz, so this will have negligible effect on the fitted velocity widths. For HCN and H^{13}CN however, the frequency range is 3.5 MHz, corresponding to velocity range 12 km s^{-1}, so that the blending of the hyperfine components would contribute to increasing the fitted velocity width.

3.4 SiO

The integrated silicon monoxide SiO 2–1 (86.85 GHz) emission is also shown in Fig. 3.

The SiO data cube and integrated image shows similar features to the CS 2–1 data, but the SiO line is weaker and, thus, has lower signal-to-noise ratio. The integrated emission peak near Sgr B2(M) shows absorption at around 65 km s^{-1}. The emission peak is at 17 47 18.9, −28 22 49, velocity 50 km s^{-1}, width 11 km s^{-1}, but

Table 4. Compilation of fitted peaks of the molecular features in the Sgr B2 complex. We are mostly considering here the spatial and velocity structure, but include in this table, for completeness, the intensity of the fitted peaks in the T_A^* scale. For some molecules with multiple transitions, where we have used the mean spatial position and velocity for higher signal-to-noise ratio, we list the intensities for the different transitions in consecutive lines, in order of frequency, as given in Table 2.

Feature/ molecule	RA (J2000)	Dec. (J2000)	Velocity ($km\,s^{-1}$)	Width ($km\,s^{-1}$)	T_A^* (K)
North ridge					
^{13}CO	17 47 24.2	−28 20 49	65	42	3.03
$C^{18}O$			63	36	0.56
CS	17 47 22.3	−28 20 49	61	57	1.01
HNC	17 47 22.0	−28 20 55	59	54	0.96
SiO	17 47 22.5	−28 21 06	58	41	0.32
HC_3N	17 47 21.0	−28 20 54	62	27	1.15
					1.48
					1.30
					1.33
CH_3CN	17 47 23.5	−28 21 01	64	41	0.37
					0.54
North cloud					
HC_3N	17 47 21.4	−28 21 29	68	23	1.48
					1.98
					1.79
					1.88
CH_3CN	17 47 21.3	−28 21 28	68	35	0.51
					0.70
CH_3OH	17 47 21.4	−28 21 20	68	25	3.53
					0.40
					0.69
					2.17
					0.81
					0.53
$^{13}CH_3OH$					0.52
HNCO	17 47 21.6	−28 21 20	65	25	2.94
					4.03
$HOCO^+$	17 47 21.1	−28 21 29	67	23	0.54
					0.60
OCS	17 47 21.3	−28 21 18	65	23	0.54
					0.68
					0.74
SO	17 47 21.3	−28 21 20	66	25	0.10
					0.56
					0.33
SO_2			68	21	0.30
N_2H^+	17 47 21.4	−28 21 23			1.39
CH_3CCH	17 47 21.5	−28 21 23	(73)	(23)	0.30
					0.46
NH_2CHO /H_2COH^+			(65)	(24)	0.16
NH_2CN			59	27	0.30
CH_2NH			66	19	0.22
H_2CS	17 47 21.4	−28 21 25	68	21	0.66
					0.29
					0.47
Near Sgr B2(N)					
$C^{18}O$	17 47 19.5	−28 22 15	68	22	1.60
HC_3N	17 47 18.7	−28 22 12	67	23	1.66
					2.29
					2.16
					2.69
CH_3CN	17 47 19.1	−28 22 12	66	30	0.72
					1.09
CH_3OH	17 47 18.8	−28 22 14	67	19	2.69
					1.05
					1.18
					1.77
					1.19
					0.32
$^{13}CH_3OH$					0.43
OCS	17 47 19.8	−28 22 12	66	21	0.62
					1.11
					1.28
SO	17 47 19.3	−28 22 08	66	27	0.35
					0.36
					0.87
SO_2			61	29	0.23
CH_3CCH	17 47 18.9	−28 22 33	(70)	(24)	0.36
					0.61
NH_2CHO /H_2COH^+	17 47 20.1	−28 22 27	(64)	(13)	0.42
NH_2CN			60	35	0.23
CH_2NH	17 47 20.0	−28 22 21	61	27	0.46
H_2CS	17 47 19.1	−28 22 23	67	20	0.67
					0.35
					0.39
Near Sgr B2(M)					
$C^{18}O$	17 47 20.3	−28 23 06	63	21	1.87
CS	17 47 19.2	−28 23 03			2.70
^{13}CS	17 47 18.7	−28 23 11	54	15	0.35
$C^{34}S$					0.64
HCO^+	17 47 20.1	−28 22 34			1.44
HCN	17 47 20.1	−28 22 32			1.66
HNC	17 47 19.8	−28 22 56			1.37
$H^{13}CO^+$			(50)	(8)	0.48
$H^{13}CN$			(47)	(12)	0.41
$HN^{13}C$			52	16	0.32
SiO	17 47 18.9	−28 22 49			0.54
CN	17 47 20.1	−28 22 50			0.74
HC_3N	17 47 18.6	−28 23 04	60	22	2.02
					2.95
					2.83
					3.72
CH_3CN	17 47 18.8	−28 23 11	61	33	0.74
					1.08
CH_3OH	17 47 18.2	−28 23 11	61	22	3.01
					0.99
					1.18
					1.91
					1.19
					0.65
$^{13}CH_3OH$					0.41
HNCO	17 47 18.2	−28 23 01	66	29	1.83
					2.97
$HOCO^+$	17 47 18.4	−28 23 21	63	22	0.23
					0.35
OCS	17 47 18.6	−28 23 08	62	21	0.54
					0.81
					0.95
SO	17 47 19.8	−28 22 56	61	20	0.59
					0.96
					1.66
SO_2	17 47 20.4	−28 23 04	52	26	1.00
N_2H^+	17 47 17.4	−28 23 06			0.92

Table 4 – *continued*

Feature/ molecule	RA (J2000)	Dec. (J2000)	Velocity ($km\,s^{-1}$)	Width ($km\,s^{-1}$)	T_A^* (K)
CH_3CCH	17 47 19.5	−28 23 22	(65)	(25)	0.39
					0.79
NH_2CHO	17 47 18.7	−28 23 31	(58)	(12)	0.40
$/H_2COH^+$					
NH_2CN			55	26	0.21
CH_2NH			59	18	0.35
H_2CS	17 47 19.2	−28 23 21	59	19	0.90
					0.51
					0.67
AlF	17 47 19.7	−28 22 56			0.29
Near Sgr B2(S)					
HC_3N	17 47 19.9	−28 23 55	58	20	1.53
					2.63
					2.45
					2.52
CH_3CN	17 47 19.9	−28 23 54	59	32	0.73
					0.94
CH_3OH	17 47 19.9	−28 23 57	59	20	2.00
					0.75
					1.10
					2.04
					1.07
					0.66
$^{13}CH_3OH$					0.42
OCS	17 47 19.5	−28 23 53	58	19	0.42
					0.58
					0.67
N_2H^+	17 47 20.1	−28 24 09			1.41
CH_3CCH	17 47 20.4	−28 24 04	(61)	(23)	0.20
					0.46
NH_2CHO			(53)	(12)	0.32
$/H_2COH^+$					
NH_2CN			55	17	0.25
H_2CS	17 47 20.2	−28 24 05	57	17	0.66
					0.43
					0.48
West ridge					
^{13}CO	17 47 14.0	−28 22 14	109	32	1.68
CS	17 47 14.9	−28 22 37	119	14	0.42
HCO^+	17 47 14.8	−28 22 36			
HCN	17 47 14.7	−28 22 34	119	24	0.63
HNC	17 47 14.9	−28 22 34	112	21	0.27
CH_3OH	17 47 15.0	−28 22 44	120	21	0.60
N_2H^+	17 47 15.1	−28 22 38	120	22	0.35
South-east peak					
CS	17 47 27.1	−28 23 13	41	20	1.53
SiO	17 47 27.1	−28 23 12	45	29	0.36
HC_3N	17 47 26.3	−28 23 04	55	23	0.70
					0.98
					0.94
					1.06
CH_3OH	17 47 26.7	−28 23 07	56	34	1.72
N_2H^+	17 47 27.2	−28 23 22	43	29	0.89

this is affected by the absorption with a second velocity component to the fit at 87 $km\,s^{-1}$, width 31 $km\,s^{-1}$, on the redshifted side of the absorption. There are also the north ridge, peak 17 47 22.5, −28 21 06, velocity 58 $km\,s^{-1}$, width 41 $km\,s^{-1}$, and the south-east 'CS peak' at 17 47 27.1, −28 23 12, velocity 45 $km\,s^{-1}$, width 29 $km\,s^{-1}$. These three peaks in integrated SiO, and the absorption near Sgr B2(M) and Sgr B2(N) are also seen in the integrated SiO image of Martin-Pintado et al. (1997). Higher resolution BIMA data of the peak near Sgr B2(M) are interpreted by Liu et al. (1998) as an outflow (like the CS data).

3.5 CN

Emission from the cyanide radical is observed in two groups of blended hyperfine components at CN 1–0 $J = 1/2$–$1/2$ (113.17 GHz) and 1–0 $J = 3/2$–$1/2$ (113.49 GHz), each of which consists of several components. The distribution of the integrated emission from the two sets of lines is very similar, so the sum of the two sets is plotted here, in Fig. 3. The most striking feature of the data is the strong absorption associated with Sgr B2(M) and Sgr B2(N) giving a deficit in the integrated emission in Fig. 3. This absorption is due to spiral arm clouds along the line of sight (Greaves & Williams 1994) against the strong continuum of the Sgr B2(M) and Sgr B2(N) cores, rather than absorption in the Sgr B2 complex itself.

Because of the multiple components, the data cubes are rather complicated with overlapping velocity and frequency structure. The $J = 3/2$–$1/2$ (113.49 GHz) data cube shows the peak near Sgr B2(M) with position 17 47 20.1, −28 22 50, velocity 94 $km\,s^{-1}$ (from the strongest component), width 19 $km\,s^{-1}$. There is also absorption over a wide velocity range down to −100 $km\,s^{-1}$, at the continuum peaks. We therefore interpret the velocity of the peak fit as being biased high due to the absorption. This is confirmed by the optically thin ^{13}CN lines having velocity around 52 $km\,s^{-1}$ (Gerin et al. 1984). There is widespread CN emission over the whole area, with velocity 52 $km\,s^{-1}$, fitted at the north ridge position, with broad lines (but the fitted velocity width of 113 $km\,s^{-1}$ includes the confusion of the multiple components). The CN emission is widespread compared to the distribution of other molecules studied here. The $J = 1/2$–$1/2$ (113.17 GHz) data cube shows deep absorption features at Sgr B2(M) and Sgr B2(N) but is too complicated to do much more interpretation, with the multiple components blended.

We also detect (Table 3) the weak lines of the ^{13}CN isotopologue $J = 1/2$–$1/2$ (108.65 GHz) and $J = 3/2$–$1/2$ (108.78 GHz) in extended emission and absorption at Sgr B2(N) and Sgr B2(M).

3.6 HC_3N

The integrated emission from cyanoacetylene HC_3N 9–8 (81.88 GHz), 10–9 (90.98 GHz), 11–10 (100.08 GHz) and 12–11 (109.17 GHz) is shown in Fig. 4. All four transitions show similar structure, which is a ridge of emission to the west of radio continuum peaks Sgr B2(N), Sgr B2(M) and Sgr B2(S), looping to the east, north of Sgr B2(N).

This is similar to the single-dish results of Lis & Goldsmith (1991) for the 12–11 transition, Chung, Ohishi & Morimoto (1994) for the 10–9 and 12–11 transitions, and de Vicente, Martin-Pintado & Wilson (1997) for the 11–10 transition. Higher resolution interferometer images of the $HC^{13}CCN$ 9–8 transition at 81.53 GHz are given by Kuan & Snyder (1996) and multiple transitions are given by de Vicente et al. (2000). The high-resolution interferometer observations of the HC_3N 1–0 transition at 9.10 GHz by Hunt et al. (1999) show weak maser emission, and so preferential emission at the radio continuum peaks. While interesting in its own right, this does not trace the molecular distribution well.

The data cubes show that the emission has several peaks with different velocities, which are merged together in the integrated emission images. We fit four peaks, from north to south, with a

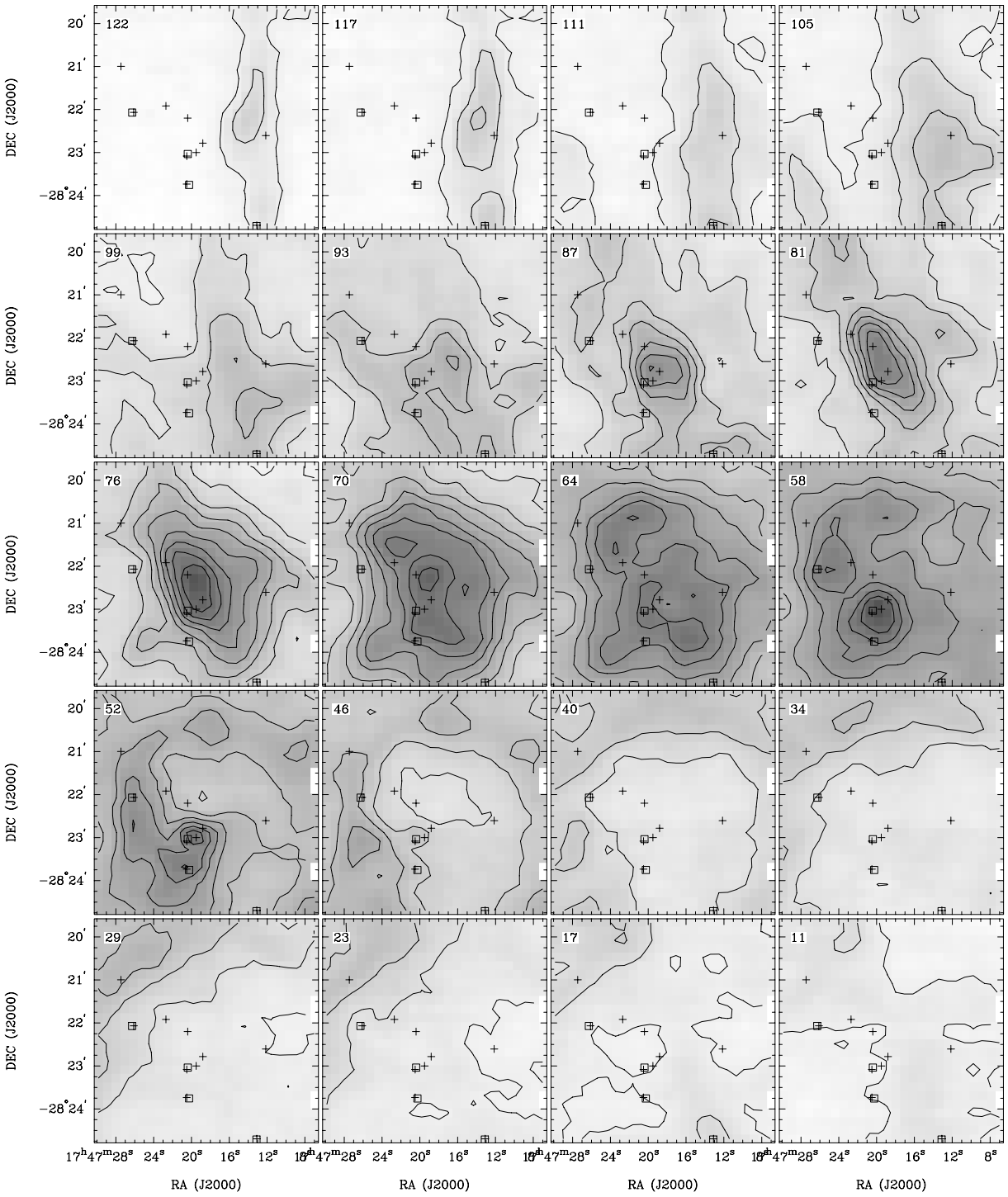

Figure 2. Velocity channel images of ^{13}CO, separated by the channel spacing of 6 km s^{-1}. Note the west ridge peaking at 117 km s^{-1}, the north ridge at 64 km s^{-1}, and how the hole at 40–50 km s^{-1} matches the clump at 70–80 km s^{-1}. The contours are steps of 0.5 K, and the peak is 5.45 K. The crosses and squares are the same as for Fig. 1.

systematic velocity gradient: (i) the north cloud at 17 47 21.4, −28 21 29, north of Sgr B2(N), velocity 68 km s^{-1}, width 23 km s^{-1}; (ii) peak at 17 47 18.7, −28 22 12, near Sgr B2(N), velocity 67 km s^{-1}, width 23 km s^{-1}; (iii) peak at 17 47 18.6, −28 23 04, near Sgr B2(M), velocity 60 km s^{-1}, width 22 km s^{-1} and (iv) peak at 17 47 19.9, −28 23 55, near Sgr B2(S), velocity 58 km s^{-1}, width 20 km s^{-1}. In addition to these four peaks we fit the north ridge at peak 17 47 21.0, −28 20 54, velocity 62 km s^{-1}, width 27 km s^{-1}, and the south-east peak at 17 47 26.3, −28 23 04, velocity 55 km s^{-1}, width 23 km s^{-1}.

We can calculate column densities of molecules in the upper level N_u from the intensities of the transitions, using the simple

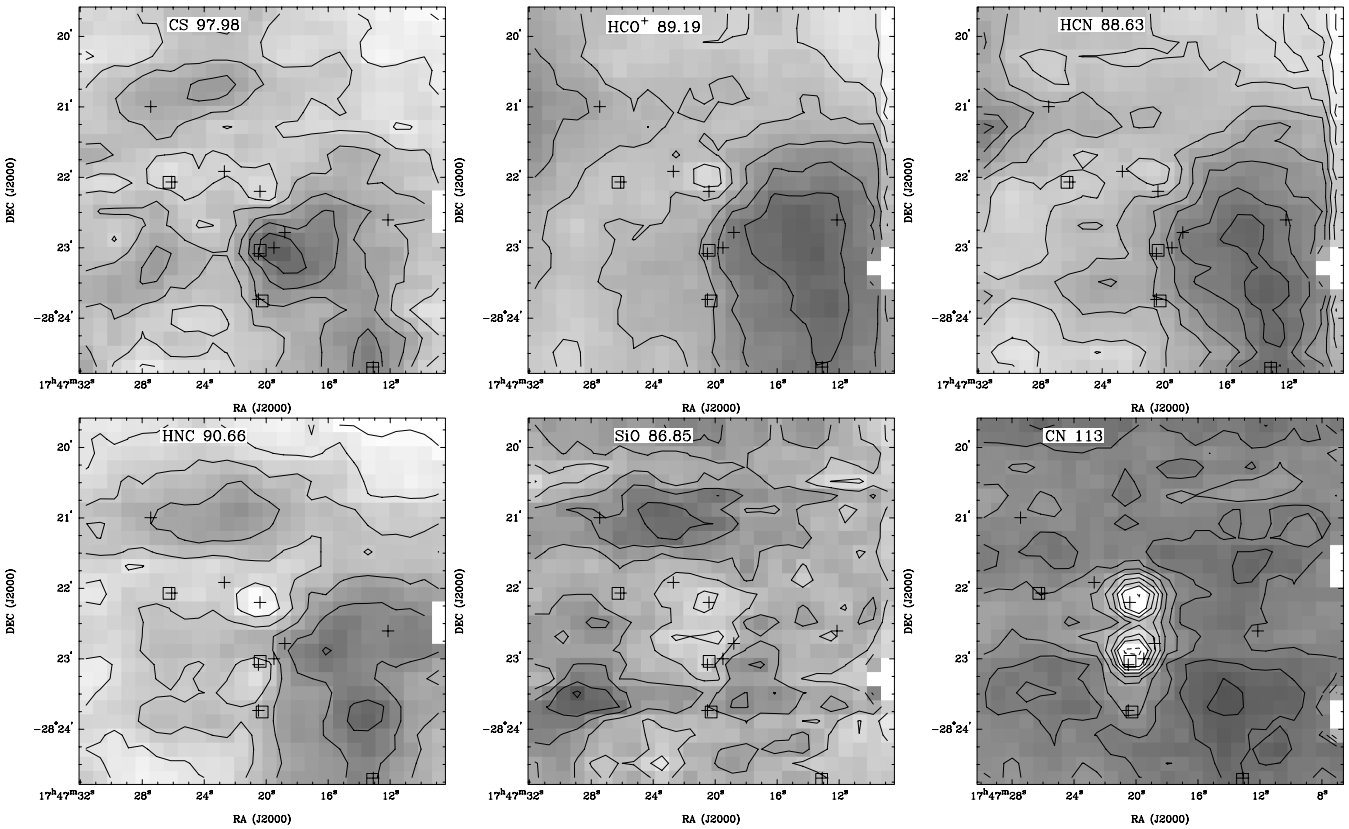

Figure 3. Integrated emission for CS (contour step 5 K km s^{-1}, peak 74 K km s^{-1}), HCO^+ (step 5 K km s^{-1}, peak 65 K km s^{-1}), HCN (step 5 K km s^{-1}, peak 94 K km s^{-1}), HNC (step 5 K km s^{-1}, peak 57 K km s^{-1}), SiO (step 2 K km s^{-1}, peak 18.4 K km s^{-1}) and CN (step 10 K km s^{-1}, peak 93 K km s^{-1}). Note that the grey-scale is darker for stronger emission, so the lighter shades near Sgr B2(N) [and Sgr B2(M) for SiO, HNC and CN] indicate lower integrated emission due to absorption.

assumption that lines are optically thin and in local thermodynamic equilibrium (LTE) by

$$N_{\rm u} = \left(8\pi\nu^2 k/hc^3 A_{\rm ul}\right) \int T_{\rm B}{\rm d}v \qquad (1)$$

where $A_{\rm ul}$ is the Einstein coefficient, and $\int T{\rm d}v$ is the integral over velocity of the brightness temperature $T_{\rm B}$ of the emission line. Using the multiple HC_3N transitions we can, in principle, plot an excitation diagram of column density in that level [expressed as $\ln(N_{\rm u}/g_{\rm u})$] versus the energy of the level (expressed as $E_{\rm u}/k$), to determine the total column density N and excitation temperature $T_{\rm ex}$, using the equation

$$(N_{\rm u}/g_{\rm u}) = (N/Q_T)\exp(-E_{\rm u}/kT_{\rm ex}), \qquad (2)$$

where Q_T is the partition function at excitation temperature $T_{\rm ex}$, and $g_{\rm u}$ is the statistical weight of the upper level. In practice, for the lines here in the 3-mm band, we do not have enough range in the energy levels for this to be very reliable ($E_{\rm u}/k$ = 20–34 K for these lines). However, we can determine that there are spatial variations in the excitation temperature, between the peaks, with the cloud north of Sgr B2(N) giving $T_{\rm ex}$ = 28 K (20–46 K in the 1σ range) and the others hotter with limits >43, >76 and >41 K (at the 1σ level) for the peaks near Sgr B2(N), Sgr B2(M) and Sgr B2(S), respectively. This is confirmed by considering the spatial variation in ratios of the different transitions, and is consistent with the results of Chung et al. (1994) and the higher kinetic temperature in these hot dense cores (de Vicente et al. 1997). This analysis is complicated towards Sgr B2(N), as the IRAM 30-m survey of Belloche et al. (2005, 2007) shows that the HC_3N is somewhat optically thick there.

We also detect (Table 3) seven vibrationally excited lines of HC_3N at 91.20, 91.33, 100.32, 100.71, 109.44, 109.60 and 109.87 GHz, concentrated at Sgr B2(N), as the higher upper energy transitions are excited in this hot region. We detect weak lines of the isotopologues $H^{13}CCCN$, $HC^{13}CCN$ and $HCC^{13}CN$ at 88.17, 90.60, 99.65 and 108.71 GHz, many of which appear to peak at Sgr B2(N), but as the lines are weak the spatial distribution is not clear.

3.7 CH_3CN

The integrated emission from methyl cyanide CH_3CN 5–4 (91.99 GHz) and 6–5 (110.38 GHz) is shown in Fig. 4. There are multiple components for each of these transitions. The integrated emission for the two sets of lines is similar, and similar to that of the four HC_3N lines. It is also similar to the single-dish results of de Vicente et al. (1997) for the 5–4 transition. We fit five components similar to that in HC_3N above: (i) the north cloud at 17 47 21.3, −28 21 28, velocity 68 km s^{-1}, width 35 km s^{-1}; (ii) peak near Sgr B2(N) at 17 47 19.1, −28 22 12, velocity 66 km s^{-1}, width 30 km s^{-1}; (iii) peak near Sgr B2(M) at 17 47 18.8, −28 23 11, velocity 61 km s^{-1}, width 33 km s^{-1}; (iv) peak near Sgr B2(S) at 17 47 19.9, −28 23 54, velocity 59 km s^{-1}, width 32 km s^{-1} and (v) the north ridge at 17 47 23.5, −28 21 01, velocity 64 km s^{-1}, width 41 km s^{-1}. The ratio of integrated emission of the two lines indicates that the peaks near Sgr B2(N) and Sgr B2(M) have higher excitation temperature than the surrounding area, but the overlapping

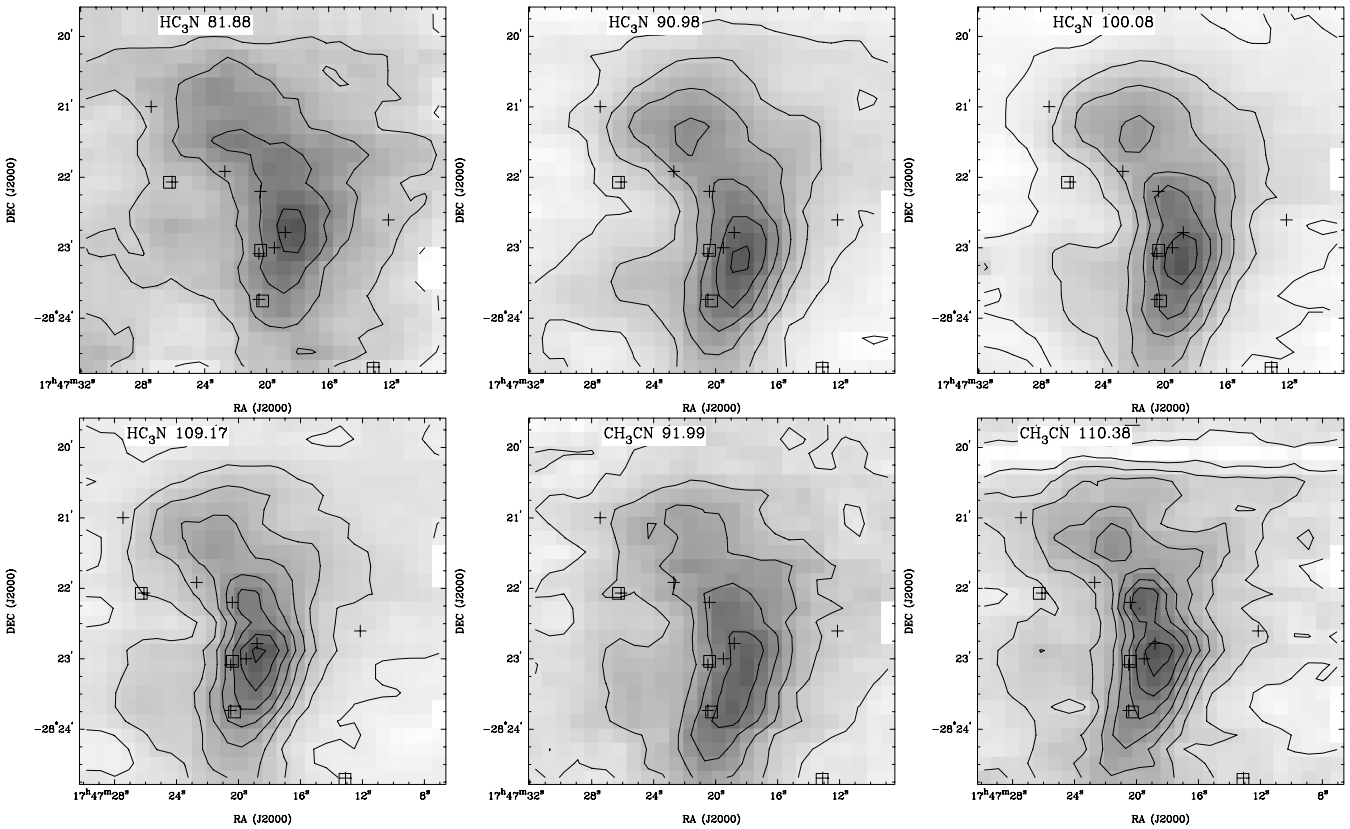

Figure 4. Integrated emission for HC_3N (contour step 10 K km s^{-1}; 81.88 GHz, peak 55 K km s^{-1}; 90.98 GHz, peak 72 K km s^{-1}; 100.08 GHz, peak 68 K km s^{-1}; 109.17 GHz, peak 83 K km s^{-1}) and CH_3CN (contour step 5 K km s^{-1}; 91.99 GHz, peak 28 K km s^{-1}; 110.38 GHz, peak 43 K km s^{-1}). These two molecules trace an arc from the north cloud, then west of the radio and mid-IR continuum peaks.

components and low signal-to-noise ratio make more quantitative analysis difficult.

We also detect weak emission (Table 3) from several more transitions of CH_3CN at 92.26, 110.33, 110.35, 110.69 and 110.71 GHz, and the isotopologues $^{13}CH_3CN$ at 107.19 GHz and possibly $CH_3^{13}CN$ at 110.33 GHz (as a blend). These are concentrated at the position of Sgr B2(N).

3.8 CH_3OH and $^{13}CH_3OH$

In Fig. 5 we show the integrated emission of five transitions of methanol CH_3OH: 5(−1,5)–4(0,4) E (84.52 GHz), 8(0,8)–7(1,7) A+ (95.17 GHz), 2(1,2)–1(1,1) A+ (95.91 GHz), 2(0,2)–1(0,1) A+ blend (96.74 GHz) and 2(1,1)–1(1,0) A− (97.58 GHz). In addition, we show the integrated emission of the isotopologue $^{13}CH_3OH$ 2(0,2)–1(0,1) A+ blend (94.41 GHz), and we have data, not plotted here for the CH_3OH 0(0,0)–1(−1,1) E (108.89 GHz) transition. The distribution of integrated emission is quite different for the different transitions.

Methanol is a very useful tracer of physical conditions, described as 'the Swiss army knife of star formation' (Leurini et al. 2005), particularly when using simultaneous fits to multiple lines (Leurini et al. 2004). However, the excitation conditions of methanol can be very complicated, with collisional and radiative excitation. For example, both the 84.52- and 95.17-GHz transitions here can be masers (Cragg et al. 1992). Also the A and E types can be considered separate species, which have different abundances. We do not attempt to model the different CH_3OH lines here, but restrict ourselves to describing their overall features.

The different lines mostly trace the same spatial and velocity structure, despite the different relative intensities of the features. These are: (i) the north cloud at 17 47 21.4, −28 21 20, velocity 68 km s^{-1}, width 25 km s^{-1}; (ii) the peak near Sgr B2(N) at 17 47 18.8, −28 22 14, velocity 67 km s^{-1}, width 19 km s^{-1}; (iii) the peak near Sgr B2(M) at 17 47 18.2, −28 23 11, velocity 61 km s^{-1}, width 22 km s^{-1} and (iv) the peak near Sgr B2(S) at 17 47 19.9, −28 23 57, velocity 59 km s^{-1}, width 20 km s^{-1}. The 96.74-GHz CH_3OH line and the 94.41-GHz $^{13}CH_3OH$ line are blends of multiple transitions, so the velocity structure is confused. The 96.74-GHz line also shows absorption at Sgr B2(N) and Sgr B2(M). Because it is the strongest line, however, it shows features not seen in the other weaker lines: the south-east peak (seen in CS) at 17 47 26.7, −28 23 07, velocity 56 km s^{-1}, width 34 km s^{-1}; the western ridge at 17 47 15.0, −28 22 44, velocity 120 km s^{-1}, width 21 km s^{-1}; and a peak to the north-west of the main ridge line at 17 47 14.5, −28 21 41, velocity 70 km s^{-1} (and width unclear due to blending with other features).

There are thirteen more weak CH_3OH lines detected here (Table 3) concentrated at the position of Sgr B2(N), that are higher upper energy lines excited in the hot core.

3.9 CH_3CH_2OH

We have also detected and imaged the ethanol CH_3CH_2OH 6(0,6)–5(1,5) (85.27 GHz) transition, but as the line is weak, and the data are affected by scanning stripes, the integrated emission is not shown here. The emission is centred on the north cloud, and the line fit gives velocity 68 km s^{-1}, width 21 km s^{-1}. We expect from

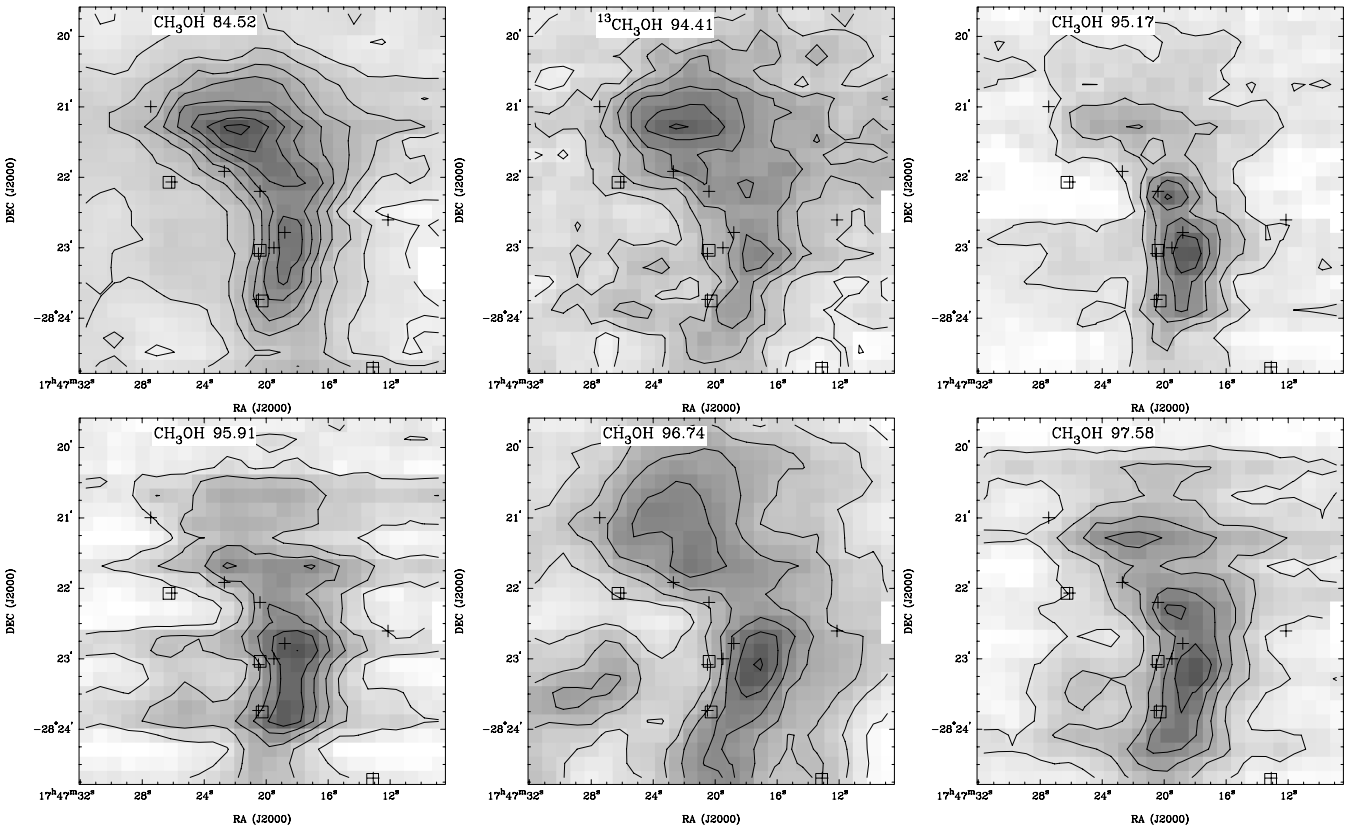

Figure 5. Integrated emission for CH_3OH (84.52 GHz, contour step 10 K km s^{-1}, peak 93 K km s^{-1}; 95.17 GHz, step 4 K km s^{-1}, peak 23 K km s^{-1}; 95.91 GHz, step 5 K km s^{-1}, peak 30 K km s^{-1}; 96.74 GHz, step 10 K km s^{-1}, peak 131 K km s^{-1}; 97.58 GHz, step 5 K km s^{-1}, peak 30 K km s^{-1}) and $^{13}CH_3OH$ (94.41 GHz, step 2 K km s^{-1}, peak 16.4 K km s^{-1}). These lines show the arc from the north cloud, west of the radio and mid-IR continuum peaks, with differences in the relative intensities of the peaks related to the complicated excitation of the different levels.

Requena-Torres et al. (2006) that the ethanol CH_3CH_2OH column density follows that of methanol CH_3OH, but the distributions of line emission here differ due to excitation differences.

The CH_3CH_2OH 7(0,7)–6(1,6) and 5(1,5)–4(0,4) (104.49 and 104.80 GHz) transitions show weak extended emission (Table 3).

3.10 HNCO

The integrated emission from isocyanic acid HNCO 4(0,4)–3(0,3) (87.93 GHz) and 5(0,5)–4(0,4) (109.91 GHz) is shown in Fig. 6. The cloud 2 arcmin north of Sgr B2(M) is particularly prominent in HNCO, as pointed out by Wilson et al. (1996) from observations of the 21.98 GHz 1–0 line, and as discussed in Minh et al. (1998) including observations, as here, of the 4(0,4)–3(0,3) and 5(0,5)–4(0,4) lines. We find similar integrated emission in the 4(0,4)–3(0,3) to Minh et al. (1998), and the velocity gradient in the data cubes, which they attribute to collapse. The 5(0,5)–4(0,4) line at 109.91 GHz here also shows the ridge west of the Sgr B2(N), Sgr B2(M) and Sgr B2(S) radio and IR continuum peaks, but the ridge is less clearly broken into clumps than in other molecules, such as HC_3N. We fit the north cloud at peak 17 47 21.6, −28 21 20, velocity 65 km s^{-1}, width 25 km s^{-1} and the peak near Sgr B2(M) at 17 47 18.2, −28 23 01, velocity 66 km s^{-1}, width 29 km s^{-1}. From the ratio of the two lines, the peak near Sgr B2(M) has a higher excitation temperature, but the difference in energy of the upper levels is too small (E_u/k = 10.5–15.8 K) to get reliable excitation temperatures from this comparison.

We detect four more weak lines of HNCO at 88.24, 109.49, 109.87 and 110.29 GHz (Table 3) concentrated at Sgr B2(N) and Sgr B2(M), which are higher upper energy transitions excited in the hot cores.

3.11 $HOCO^+$

The integrated emission from protonated CO_2 $HOCO^+$ 4(0,4)–3(0,3) (85.53 GHz) is shown in Fig. 6. The distribution is similar to that of HNCO, with the north cloud prominent, as also shown in Minh, Irvine & Ziurys (1988) and Minh et al. (1998). We also have data for the 5(0,5)–4(0,4) (106.91 GHz) transition, but this is not shown here, as the image is qualitatively similar, but poorer quality, being affected by scanning stripes. There is a ridge west of Sgr B2(N), Sgr B2(M) and Sgr B2(S), similar to that for HNCO. We fit the north cloud as peak 17 47 21.1, −28 21 29, velocity 67 km s^{-1}, width 23 km s^{-1}, and the peak near Sgr B2(M) at 17 47 18.4, −28 23 21, velocity 63 km s^{-1}, width 22 km s^{-1}. We also find the peak near Sgr B2(M) has a higher excitation temperature, from the ratio of the peaks in the two lines. The difference in energy of the upper levels is however too small (E_u/k = 10.3–15.4 K) for the calculated excitation temperatures to be very reliable, but the data do suggest higher excitation temperatures than the 13 K of Minh et al. (1988).

3.12 OCS

The integrated emission from carbonyl sulphide OCS 7–6 (85.14 GHz), 8–7 (97.30 GHz) and 9–8 (109.46 GHz) is shown

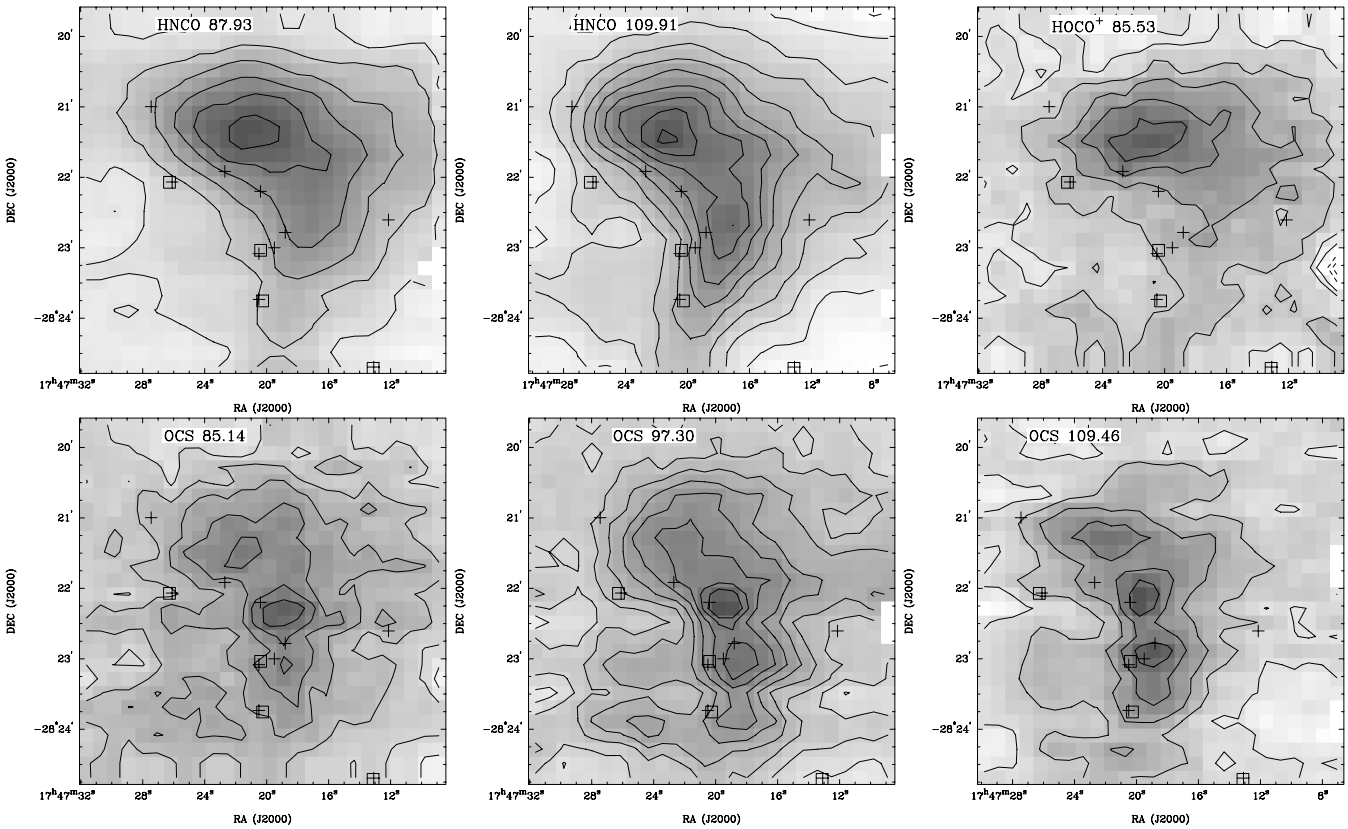

Figure 6. Integrated emission for HNCO (contour step 10 K km s^{-1}; 87.93 GHz, peak 84 K km s^{-1}; 109.91 GHz, peak 113 K km s^{-1}), $HOCO^+$ (85.53 GHz, step 2 K km s^{-1}, peak 13.4 K km s^{-1}) and OCS (85.14 GHz, step 2 K km s^{-1}, peak 15.6 K km s^{-1}; 97.30 GHz, step 2 K km s^{-1}, peak 24 K km s^{-1}; 109.46 GHz, step 4 K km s^{-1}, peak 24 K km s^{-1}).

in Fig. 6. The emission traces the north cloud, and ridge line, with the peaks near Sgr B2(N), Sgr B2(M) and Sgr B2(S) quite compact and hence distinct in the integrated emission. This is unlike the more continuous ridge line seen in HC_3N (Fig. 4), as shown by the higher resolution data from Goldsmith et al. (1987) for the OCS 9–8 and HC_3N 12–11 transitions. We fit (i) the north cloud at peak 17 47 21.3, −28 21 18, velocity 65 km s^{-1}, width 23 km s^{-1}; (ii) the peak near Sgr B2(N) at 17 47 19.8, −28 22 12, velocity 66 km s^{-1}, width 21 km s^{-1}; (iii) the peak near Sgr B2(M) at 17 47 18.6, −28 23 08, velocity 62 km s^{-1}, width 21 km s^{-1} and (iv) the peak near Sgr B2(S) at 17 47 19.5, −28 23 53, velocity 58 km s^{-1}, width 19 km s^{-1}. Despite having three transitions, we cannot get reliable excitation temperatures due to the small range of upper energy levels ($E_u/k =$ 16.3–26.3 K) and the low signal-to-noise ratio, but we do note that the peaks near Sgr B2(N) and Sgr B2(M) have higher excitation temperatures than the north cloud.

We also detect (Table 3) the $O^{13}CS$ 9–8 line at 96.98 GHz, which has a similar extended distribution, with the strongest peak near Sgr B2(N), although the IRAM 30-m survey of Belloche et al. (2005, 2007) indicates this line is blended with several other lines at Sgr B2(N) and Sgr B2(M).

3.13 SO

The integrated emission from sulphur monoxide SO 2(2)–1(1) (86.09 GHz), 3(2)–2(1) (99.30 GHz) and 2(3)–1(2) (109.25 GHz) is shown in Fig. 7. The distribution of the 86.09- and 109.25-GHz transitions is similar, with compact peaks near Sgr B2(N) and Sgr B2(M), as shown by Goldsmith et al. (1987) at higher resolution for the 109.25-GHz transition. The 99.30-GHz transition, however, shows quite a different distribution tracing the north cloud and ridge line to the west, and with absorption in the data cube at Sgr B2(N) and Sgr B2(M). This is presumably because the 86.09- and 109.25-GHz transitions trace the more excited gas ($E_u/k = 19.3$ and 21.0 K) than the 99.30-GHz transition ($E_u/k = 9.2$ K). We fit (i) the north cloud (99.30 GHz) at peak 17 47 21.3, −28 21 20, velocity 66 km s^{-1}, width 25 km s^{-1}; (ii) peak near Sgr B2(N) (86.09 and 109.25 GHz) at 17 47 19.3, −28 22 08, velocity 66 km s^{-1}, width 27 km s^{-1} and (iii) peak near Sgr B2(M) at 17 47 19.8, −28 22 56, velocity 61 km s^{-1}, width 20 km s^{-1}.

We also detect (Table 3) the SO 4(5)–4(4) line at 100.03 GHz, concentrated at Sgr B2(M) and Sgr B2(N), and the isotopologue ^{34}SO 3(2)–2(1) and 2(3)–1(2) lines at 97.72 and 106.74 GHz, at Sgr B2(M).

3.14 SO_2

The integrated emission from sulphur dioxide SO_2 3(1,3)–2(0,2) (104.03 GHz) is also shown in Fig. 7. The peak near Sgr B2(M) dominates, but there is also weak emission seen from the north cloud. The peak near Sgr B2(M) is at 17 47 20.4, −28 23 04, velocity 52 km s^{-1}, width 26 km s^{-1}, which is lower velocity here than as seen in other lines. The north cloud has velocity 68 km s^{-1}, width 21 km s^{-1}, and near Sgr B2(N) velocity 61 km s^{-1}, width 29 km s^{-1}. The low-level east–west extension is an artefact of the east–west scanning and baseline variations.

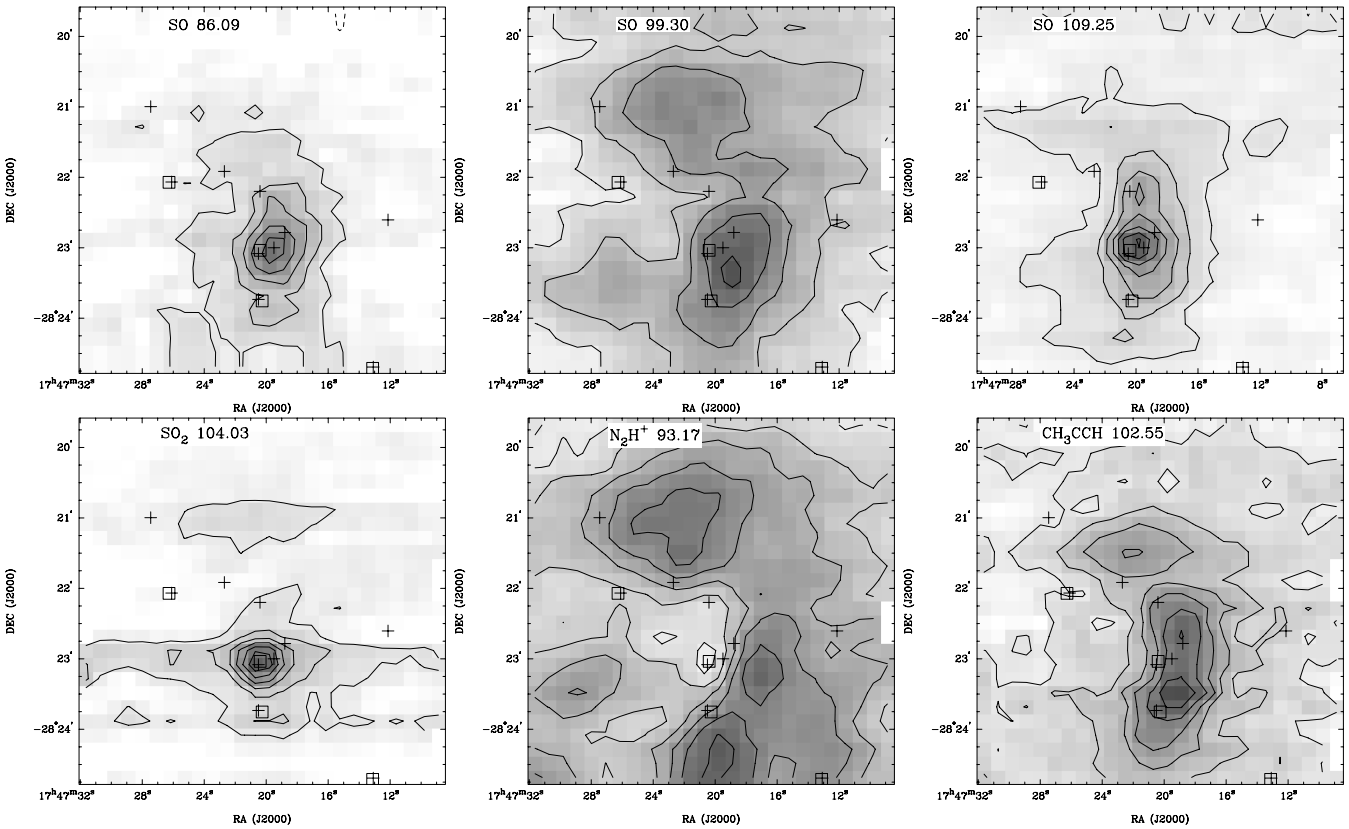

Figure 7. Integrated emission for SO (86.09 GHz, contour step 2 K km s^{-1}, peak 11.1 K km s^{-1}; 99.30 GHz, step 4 K km s^{-1}, peak 25 K km s^{-1}; 109.25 GHz, step 5 K km s^{-1}, peak 36 K km s^{-1}), SO_2 (step 5 K km s^{-1}, peak 35 K km s^{-1}), N_2H^+ (step 5 K km s^{-1}, peak 52 K km s^{-1}) and CH_3CCH (step 5 K km s^{-1}, peak 35 K km s^{-1}).

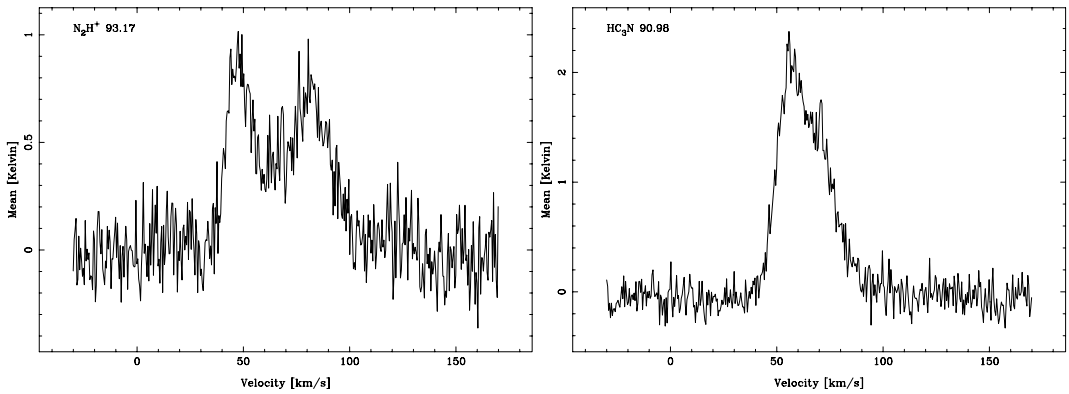

Figure 8. Spectra of N_2H^+ and HC_3N near Sgr B2(M) illustrating how some spectral lines show absorption at around 60 km s^{-1}, from gas seen in emission at this velocity in other lines. There are multiple components to the N_2H^+ line, which contributes to broadening the line, but the frequency range is too small to explain the double profile.

We detect eight more lines of SO_2 at 83.69, 91.55, 97.70, 100.88, 104.24, 107.06, 107.84 and 109.75 GHz (Table 3) concentrated at Sgr B2(N) and Sgr B2(M).

3.15 N_2H^+

The integrated emission from diazenylium N_2H^+ 1–0 (93.17 GHz) is shown in Fig. 7. The data cube shows complicated structure, with deep absorption at Sgr B2(N) and Sgr B2(M) at around 66 km s^{-1}, and double-peaked spectra over most of the area (Fig. 8), which we attribute to widespread absorption at a similar velocity. There are multiple components to the 1–0 line, which contributes to broadening the fitted linewidth, but the frequency range is too small to explain the double profiles. The major features are fitted as (i) the north cloud at 17 47 21.4, −28 21 23, velocity 51 and 81 km s^{-1}; (ii) peak to the west of Sgr B2(M) at 17 47 17.2, −28 23 06, velocity 47 and 79 km s^{-1}; (iii) peak south of Sgr B2(S) at 17 47 20.1, −28 24 09, velocity 46 and 71 km s^{-1}; (iv) west ridge at 17 47 15.1, −28 22 38, velocity 120 km s^{-1}, width 22 km s^{-1} and (v) south-east peak at 17 47 27.2, −28 23 22, velocity 43 km s^{-1}, width 29 km s^{-1}.

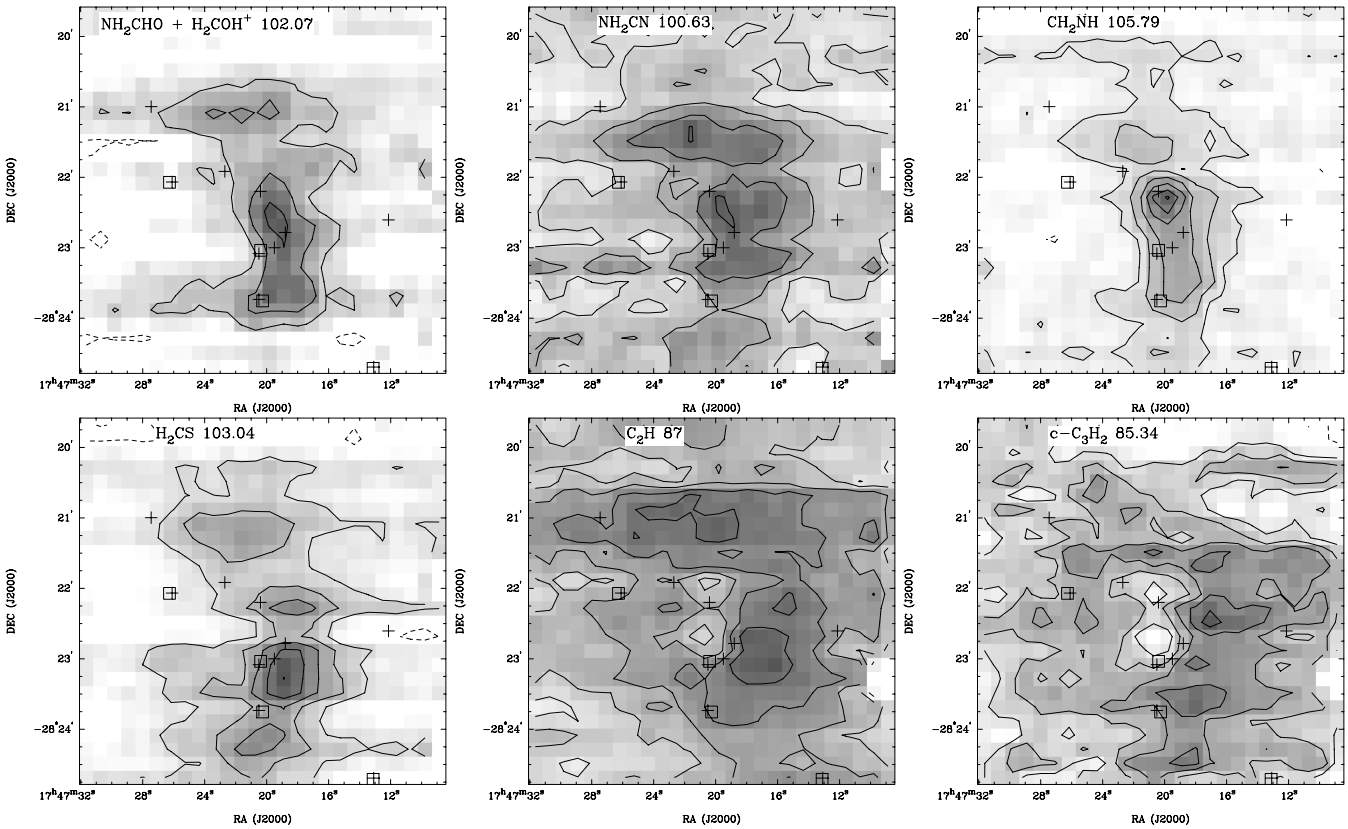

Figure 9. Integrated emission for NH_2CHO blended with H_2COH^+ (contour step 2 K km s^{-1}, peak 6.6 K km s^{-1}), NH_2CN (step 2 K km s^{-1}, peak 8.4 K km s^{-1}), CH_2NH (step 2 K km s^{-1}, peak 12.3 K km s^{-1}), H_2CS (103.04 GHz, step 2 K km s^{-1}, peak 10.0 K km s^{-1}), C_2H (step 5 K km s^{-1}, peak 40 K km s^{-1}) and c-C_3H_2 (step 2 K km s^{-1}, peak 11.1 K km s^{-1}).

3.16 CH_3CCH

The integrated emission from propyne or methyl acetylene CH_3CCH 6–5 (102.55 GHz) is shown in Fig. 7. We also have data for the CH_3CCH 5–4 (85.46 GHz) transition, not shown here as it is qualitatively similar, but weaker and noisier. The distribution shows the north cloud, and ridge line west of the radio continuum peaks. The fitted features are: (i) the north cloud at 17 47 21.5, −28 21 23, velocity 73 km s^{-1}, width 23 km s^{-1}; (ii) peak near Sgr B2(N) and Sgr B2(M) at 17 47 18.9, −28 22 33, velocity 70 km s^{-1}, width 24 km s^{-1}; (iii) peak near Sgr B2(M) and Sgr B2(S) at 17 47 19.5, −28 23 22, velocity 65 km s^{-1}, width 25 km s^{-1} and (iv) peak south of Sgr B2(S) at 17 47 20.4, −28 24 04, velocity 61 km s^{-1}, width 23 km s^{-1}. There are multiple blended line components, so the spectra are a fit to the line blend with the velocity calculated using the rest frequency of one of the components. The velocity therefore is offset, but the gradient is shown, similar to that found in CH_3CCH by Churchwell & Hollis (1983) with lower resolution, but over a larger area.

3.17 NH_2CHO and H_2COH^+

The integrated emission from the line at 102.07 GHz is shown in Fig. 9. We identify this as a blend of formamide NH_2CHO 5(1,5)–4(1,4) and protonated formaldehyde H_2COH^+ 4(0,4)–3(1,3), as noted by Ohishi et al. (1996). We identify four peaks, as for other lines like CH_3CCH 6–5 (102.55 GHz) above, but because the line is weak, we do not get good positional fits for all of them. The features are: (i) the north cloud with velocity 65 km s^{-1}, width 24 km s^{-1}; (ii) peak near Sgr B2(N) and Sgr B2(M) at 17 47 20.1, −28 22 27, velocity 64 km s^{-1}, width 13 km s^{-1}; (iii) peak near Sgr B2(M) and Sgr B2(S) at 17 47 18.7, −28 23 31, velocity 58 km s^{-1}, width 12 km s^{-1} and (iv) peak south of Sgr B2(S) with velocity 53 km s^{-1}, width 12 km s^{-1}. The velocities are calculated using the rest frequency of NH_2CHO 5(1,5)–4(1,4), so again will be shifted due to the blending.

We detect eight more weak lines of NH_2CHO at 85.09, 87.85, 93.87, 105.46, 105.97, 106.13, 106.54 and 109.75 GHz (Table 3). The spatial distribution shows excitation differences, with some of these concentrated at Sgr B2(N), and others extended in the north–south ridge line a bit to the west. This is consistent with higher upper energy lines being excited in the hot core, although complicated by several of the lines being blended with other species.

3.18 NH_2CN

The integrated emission from cyanamide NH_2CN 5(1,4)–4(1,3) (100.63 GHz) is shown in Fig. 9. The line is rather weak, and the data affected by scanning ripples, so we do not fit the positions, but we do see the four peaks in the data cube and fit velocities: (i) the north cloud with velocity 59 km s^{-1}, width 27 km s^{-1}; (ii) peak near Sgr B2(N) and Sgr B2(M) with velocity 60 km s^{-1}, width 35 km s^{-1}; (iii) peak near Sgr B2(M) and Sgr B2(S) with velocity 55 km s^{-1}, width 26 km s^{-1} and (iv) peak south of Sgr B2(S) with velocity 55 km s^{-1}, width 17 km s^{-1}.

3.19 CH_2NH

The integrated emission from methylenimine CH_2NH 4(0,4)–3(1,3) (105.79 GHz) is shown in Fig. 9. The peak close to Sgr B2(N) is strong, and we detect the north cloud and the ridge line, with fits: (i) the north cloud with velocity 66 km s^{-1}, width 19 km s^{-1}; (ii) peak near Sgr B2(N) at 17 47 20.0, −28 22 21, velocity 61 km s^{-1}, width 27 km s^{-1} and (iii) peak near Sgr B2(M) and Sgr B2(S) with velocity 59 km s^{-1}, width 18 km s^{-1}. This line is probably blended with HC^{13}CCN 12–11 at rest frequency 105.799 093 GHz.

3.20 H_2CS

The integrated emission from thioformaldehyde H_2CS 3(0,3)–2(0,2) (103.04 GHz) is shown in Fig. 9. We also have data (not plotted here as the images are similar, but noisy) for H_2CS 3(1,3)–2(1,2) (101.48 GHz) and 3(1,2)–2(1,1) (104.62 GHz). We fit four peaks as (i) the north cloud at 17 47 21.4, −28 21 25, velocity 68 km s^{-1}, width 21 km s^{-1}; (ii) peak near Sgr B2(N) at 17 47 19.1, −28 22 23, velocity 67 km s^{-1}, width 20 km s^{-1}; (iii) peak near Sgr B2(M) and Sgr B2(S) at 17 47 19.2, −28 23 21, velocity 59 km s^{-1}, width 19 km s^{-1} and (iv) peak south of Sgr B2(S) at 17 47 20.2, −28 24 05, velocity 57 km s^{-1}, width 17 km s^{-1}.

3.21 C_2H

The integrated emission from ethynyl C_2H 1–0 $J = 1/2$–$1/2$ (87.32 GHz) and 1–0 $J = 3/2$–$1/2$ (87.40 GHz), is shown in Fig. 9. As for CN, above, each set consists of components and the integrated emission of two sets of lines is very similar, but weak, so the sum of the two sets is plotted here. The integrated emission image in Fig. 9 shows widespread emission peaked at the north ridge and west of Sgr B2(M), and a deficit of emission at the continuum peaks Sgr B2(N) and Sgr B2(M). The fitting of velocity components in the data cubes is complicated by the blended components, and the weakness of the emission, but the emission is peaked around 60–65 km s^{-1}. The deficit of integrated emission near Sgr B2(N) and Sgr B2(M) could be explained by a real deficit of the molecule in this area, but is more likely simply be due to absorption, as Greaves & Nyman (1996) show absorption features due to intervening clouds along the line of sight to Sgr B2. The offset between the absorption and the radio continuum peaks is not considered significant, but rather due to the baseline stripes in the east–west scanning direction causing north–south shifts in centres of the weak features.

3.22 *c*-C_3H_2

The integrated emission from the cyclic molecule cyclopropenylidene *c*-C_3H_2 2(1,2)–1(0,1) (85.34 GHz) is shown in Fig. 9. This shows similar features to C_2H, that is widespread emission with a deficit at continuum peaks Sgr B2(N) and Sgr B2(M). The emission is weak, however, so the integrated emission does show some spurious striping due to the RA scanning. Vrtilek, Gottlieb & Thaddeus (1987) find rotation temperature $T_{\rm rot} = 11 \pm 2$ K for *c*-C_3H_2 in Sgr B2, so absorption against the continuum is quite plausible. As for C_2H, above, the position offset between the absorption and continuum peaks is not considered significant.

3.23 Other molecules

We list in Table 3 nine more molecules, and dozens more lines, than we have plotted and discussed above, as well as weaker transitions of the molecules already discussed. Most of these lines are confined to Sgr B2(N) or Sgr B2(M). Some of the weaker transitions are higher energy states, some vibrationally excited, of molecules already discussed, which trace these hot cores.

Since the main aim of this paper is the wider scale spatial distribution, we do not concentrate here on quantitative analysis of the weaker lines. Our Mopra OTF mapping sacrifices sensitivity on a single position to get the spatial coverage. Therefore our data on the spectra at the Sgr B2(N) and Sgr B2(M) positions are not particularly sensitive compared to previous (Turner 1989) and current (Belloche et al. 2005; Hieret et al. 2005; Belloche et al. 2007) dedicated spectral-line surveys of these well-studied sources. However, by mapping it is useful to determine whether a particular line is confined to Sgr B2(N), Sgr B2(M), or both, or whether it is distributed more widely. Of the weaker lines (Table 3) a substantial fraction are identified with blends of different species, complicating the analysis.

Four molecules in Table 3 have extended spatial distribution: acetaldehyde CH_3CHO (93.60, 95.95, 95.96 and 98.90 GHz), dicarbon monosulphide CCS (93.87 and 106.35 GHz), methanethiol CH_3SH (101.03 and 101.14 GHz) and ketene CH_2CHO (101.03 GHz). These distributions appear similar to that of some other molecules, such as HC_3N, with the north cloud and ridge line to the west of the radio continuum peaks, but with much lower signal-to-noise ratio.

The other five molecules are confined to Sgr B2(N), as this region is known to be particularly rich in large molecules (Snyder et al. 1994; Miao et al. 1995). These molecules are: ethyl cyanide or propionitrile CH_3CH_2CN (22 lines), acrylonitrile CH_2CHCN (92.43, 94.28, 94.91, 95.33, 103.57, 104.21 and 106.64 GHz), methyl formate CH_3OCHO (89.32, 98.18 and 107.54 GHz), dimethyl ether CH_3OCH_3 (82.46, 100.46 and 105.77 GHz) and formaldehyde H_2CO (101.33 GHz).

More sensitive observations of Sgr B2(N) and Sgr B2(M) with the IRAM 30-m (Belloche et al. 2005, 2007) have been modelled with the XCLASS software (Comito et al. 2005), which simultaneously fits multiple lines with the LTE approximation and handles line blends well. We note here that for Sgr B2(N), in particular, this allows us to identify some extra lines that may confuse the Mopra images. These lines are: CH_2CH_3CN 10(1,10)–9(1,9) at 86.819 848 GHz for SiO; CH_2CHCN multiplet around 85.532 9236 GHz for $HOCO^+$; HC_3N 12–11 $\nu_5 = 1\, l = 1$ f at 109.244 339 GHz for SO; CH_2CHCN 9(1,8)–8(1,7) at 87.312 827 GHz for C_2H. However, the effect of this line confusion does not appear to be significant.

4 DISCUSSION

We now consider the comparison of spatial and velocity structure in the Sgr B2 complex, as traced by the different 3-mm lines. Fig. 10 shows the positions of the molecular peaks listed in Section 3, and Table 4 lists these fitted peaks.

The strongest lines, such as ^{13}CO, C^{18}O, CS, HCN, HCO^+, HNC, SiO, N_2H^+ and CH_3OH (96.74 GHz) show up three features which we have called here the north ridge, the west ridge and the south-east peak (Tables 4 and 5). These features are detected in the strongest transitions, which are also the lines which are optically thick in the densest regions of the complex [near Sgr B2(N) and (M)], so the relative prominence of these three features (Fig. 2) is partly due to this optical depth effect. However, they do trace the weaker surrounding structure of the complex. We have not imaged a large enough area to show the 'hole' around 40 km s^{-1} (Sato et al. 2000; Hasegawa et al. 2008) well, so we do not consider the wider surrounding structure.

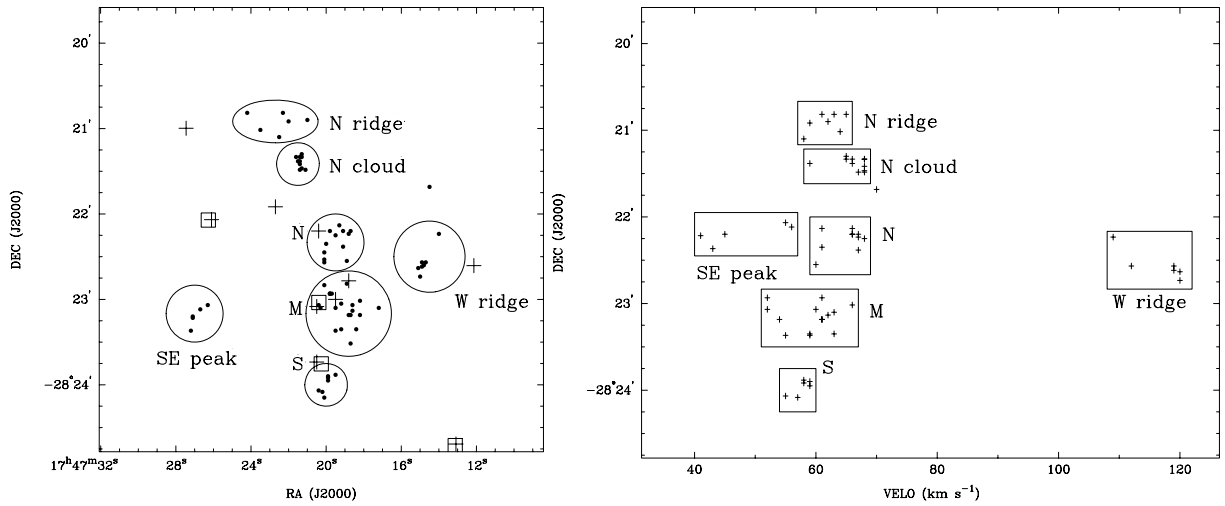

Figure 10. The position (left-hand panel) of the peaks fitted for the 3-mm molecular lines, and (right-hand panel) the velocity as a function of Dec. Note that in the velocity–Dec. plot, the points for the south-east peak have been shifted 1 arcmin north for clarity, to avoid overlapping the points near Sgr B2(M). In the left-hand diagram, the points are the 3-mm molecular peaks, the crosses radio sources and the open boxes mid-IR sources.

Table 5. Summary of molecular features in the Sgr B2 complex, from the Mopra 3-mm peaks. We give the mean and standard deviation of position, velocity and velocity width, from the fits to different lines, and include positions in Galactic coordinates for reference.

Feature	RA (J2000)	Dec. (J2000)	σ(RA) (arcsec)	σ(Dec.) (arcsec)	latitude (°)	longitude (°)	Velocity (km s^{-1})	σ(velocity) (km s^{-1})	Width (km s^{-1})	σ(Width) (km s^{-1})
North ridge	17 47 22.6	−28 20 56	15	7	0.702	−0.024	62	3	43	10
North cloud	17 47 21.4	−28 21 24	2	4	0.693	−0.024	66	3	24	4
Near Sgr B2(N)	17 47 19.3	−28 22 18	7	8	0.676	−0.026	65	3	25	5
Near Sgr B2(M)	17 47 19.2	−28 23 04	11	15	0.665	−0.032	59	4	22	5
Near Sgr B2(S)	17 47 20.0	−28 24 00	4	6	0.653	−0.043	58	2	21	6
West ridge	17 47 14.8	−28 22 34	5	9	0.664	−0.014	117	5	22	6
South-east peak	17 47 26.9	−28 23 12	5	7	0.678	−0.057	48	7	27	6

We note that the south-east peak is much more obvious in the CS, than in say ^{13}CO or C^{18}O, as noted by Yusef-Zadeh et al. (1996), indicating that there is a chemical difference from the main sources.

The west ridge and south-east peak are offset both spatially and in velocity (at around 117 and 48 km s^{-1}, respectively) from the main north–south axis of the Sgr B2 complex. The other features (Table 5), that we have called the north ridge, the north cloud, and the three groups of peaks near Sgr B2(N), Sgr B2(M) and Sgr B2(S) are in a north–south line, with a velocity gradient, as shown on the right-hand side of Fig. 10 and in Table 5.

The north ridge is (as noted) seen only in the strongest lines, while the other four features are best traced by weaker, optically thin lines. We find a spatial and velocity difference between the north ridge, and nearby chemically enriched (Minh et al. 1998) north cloud. The north ridge is elongated east–west, so there is a scatter of the peak positions along this axis, but the north cloud has a surprisingly tight distribution of peaks fitted from the different lines.

The feature near Sgr B2(S) also has a fairly tight distribution of fitted peak positions, given the 36–39 arcsec beam size of the observations. However, there is a significant difference in the peak positions, for the groups of fitted peaks near Sgr B2(N) and Sgr B2(M). This is attributed to a real difference in the positions of the peaks in different lines, where some more excited lines are associated with the compact hot cores Sgr B2(N) and Sgr B2(M), or particularly for Sgr B2(N) some molecules are concentrated there. Other lower excitation lines peak in the ridge further to the west of Sgr B2(N) and Sgr B2(M) and avoid the hot core positions as the molecules are destroyed there. The excitation effect can be seen clearly in the SO lines (Fig. 7) where the 86.09- and 109.25-GHz lines are concentrated at Sgr B2(M), while the 99.30-GHz line traces the ridge line more to the west.

From some of the stronger lines in Table 3 which are concentrated at Sgr B2(N) and Sgr B2(M) we fit the hot core positions and

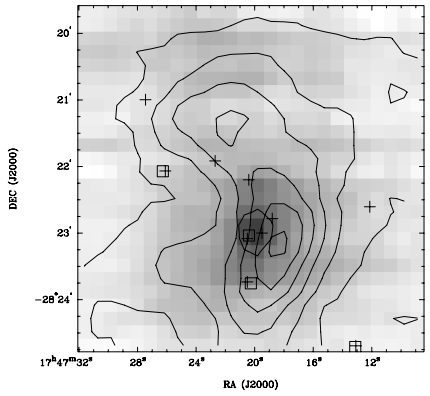

Figure 11. The C^{18}O integrated emission as grey-scale, with the 90.98 GHz HC_3N integrated emission as contours, showing how molecules such as HC_3N peak in the ridge line to the west of the hot cores.

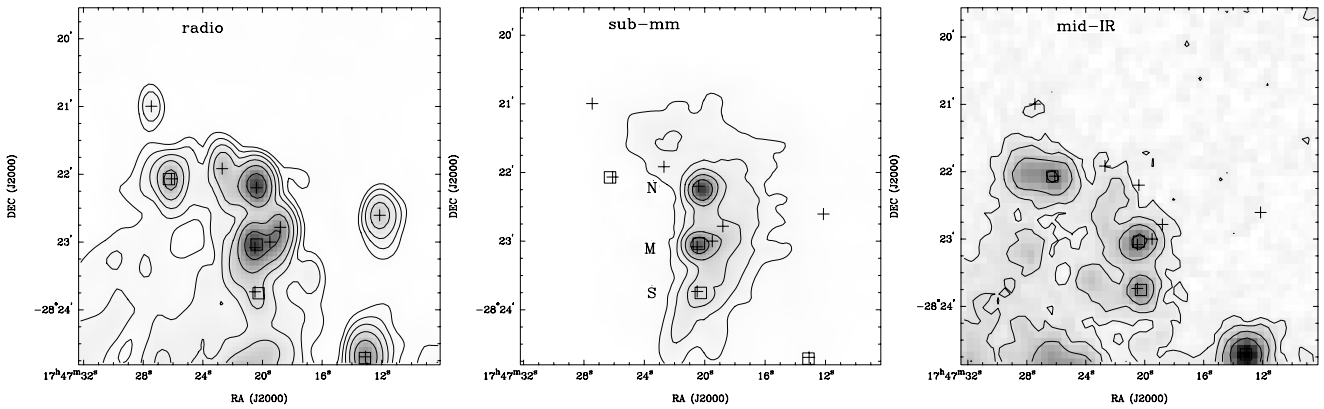

Figure 12. The continuum emission in radio (left-hand panel) from the VLA at 20-cm, submillimetre (middle panel) from SCUBA at 850 μm and mid-IR (right-hand panel) from *MSX* at 21 μm. The overlaid crosses are for radio sources and open squares for mid-IR sources. Note how the submillimetre traces diffuse cool dust to the west and north of the Sgr B2(N), (M) and (S) cores, as well as compact emission from the cores. The radio and mid-IR trace star formation in the cores and to the south-east.

velocities as: Sgr B2(N) 17 47 19.9, −28 22 11, velocity 63 km s^{-1}, width 24 km s^{-1}; and Sgr B2(M) 17 47 20.3, −28 22 58, velocity 59 km s^{-1}, width 22 km s^{-1}. From these lines [mostly CH_3OH and CH_3CH_2CN for Sgr B2(N) and SO and SO_2 for Sgr B2(M)] we find that the hot cores are unresolved relative to the 36–39 arcsec Mopra beam.

The distribution of optically thin $C^{18}O$, which should be a good tracer of CO column density, and hence H_2 column density, peaks at the Sgr B2(N) and Sgr B2(M) cores, whereas there are several molecules, such as HC_3N, CH_3CN, CH_3OH and OCS, which peak in the ridge line to the west of the cores. This is shown in Fig. 11, and in the integrated emission images, by the alignment of the distributions relative to the reference crosses (radio peaks) and squares (mid-IR peaks).

We also show in Fig. 12 the 20-cm radio, from the VLA,[4] the 850-μm submillimetre from SCUBA[5] and 21-μm mid-IR, from *MSX*.[6]

We point out that, for the many molecules here that peak in the ridge line to the west of the Sgr B2(N) and Sgr B2(M) cores, this distribution of molecular emission 'wraps around' the north and west side, where there is little radio and mid-IR emission tracing recent star formation, and avoids the south-east area where there is recent star formation. The north cloud, in particular, is quite isolated from the recent star formation activity. In contrast, the SCUBA submillimetre emission, tracing cooler dust than the mid-IR, shows extended emission around the Sgr B2(N) and Sgr B2(M) cores, to the north and west which matches well the north cloud and the molecular ridge line.

Each line that we have imaged here has its own particular distribution, corresponding to the spatial distribution of the molecule, and the effect of the excitation of the different levels. There is also a complicated velocity structure in the region. However, we can make some generalizations and comments here to bring some order to the overall results.

The CO (^{13}CO, $C^{18}O$ and $C^{17}O$) shows that the densest region is around Sgr B2(M) at velocity 63 km s^{-1}. The ^{13}CO is optically thick at this core, so the density there is better traced by the $C^{18}O$. The column density, would be further concentrated at Sgr B2(N) and Sgr B2(M), than the $C^{18}O$ 1–0 integrated line emission shown here. The higher temperature at the cores (∼200 K, compared to ∼20 K for the surrounding gas) leads to an extra factor there, when converting, with the standard LTE analysis, from integrated line emission to total CO column density, and hence total H_2 column density.

The HCO^+, HCN and HNC are strong and widespread with absorption at the Sgr B2(M) and Sgr B2(N) cores. The column density is likely to be peaked at these cores, but the integrated emission is strongly affected by this absorption, leading to local minima in the emission intensity at the cores. There are differences in the detailed distribution of these three lines, as expected: HCN should be a good tracer of high gas density ($\geqslant 10^4$ cm^{-3}), the isomer HNC should trace cool quiescent gas, and the ion HCO^+ should trace ionization due to cosmic rays. We have further Mopra data of these lines over a larger area, from broad-band observations over the 85.3–93.3 GHz range, which show the differences more clearly, so we postpone further discussion for a later paper.

The CS and SiO distributions are also affected by absorption at the Sgr B2(M) and Sgr B2(N) cores, so the column density distribution is hard to determine from the integrated emission images. CS is expected to be, like HCN, a good tracer of high density gas, and SiO is expected to trace shocks, but is quite widespread here.

The CN emission is quite uniform over the 5 × 5-arcmin^2 area observed here, except for the absorption at the Sgr B2(M) and Sgr B2(N) cores. It is expected to be associated with an enhanced ultraviolet (UV) field, so this would indicate a widespread UV field in the Sgr B2 complex. The weak lines of C_2H and c-C_3H_2 also have absorption at the Sgr B2(M) and Sgr B2(N) cores and widespread emission, but some excess emission on the ridge line west of the cores.

Most of the lines imaged here trace the ridge line west of the Sgr B2(M), Sgr B2(N) and Sgr B2(S) cores, and north-east to what we are calling the north cloud. These lines include HC_3N, CH_3CN, CH_3OH, HNCO, OCS, N_2H^+, CH_3CCH, NH_2CHO/H_2COH^+, NH_2CN, CH_2NH and H_2CS. These more complex molecules, as noted above, trace the cooler dust seen at submillimetre wavelengths, and avoid the areas with the warmer dust (mid-IR) and radio continuum associated with the active star formation. N_2H^+ and the 96.74-GHz transition of CH_3OH are strong, and also show some absorption at the Sgr B2(M) and Sgr B2(N) cores.

[4] http://imagelib.ncsa.uiuc.edu/imagelib.html.
[5] http://www3.cadc-ccda.hia-iha.nrc-cnrc.gc.ca/jcmt/.
[6] http://irsa.ipac.caltech.edu/applications/MSX/.

The relative prominence of the peaks in the ridge line west of the Sgr B2(M), Sgr B2(N) and Sgr B2(S) cores in these different molecules, and between different transitions of the same molecule (e.g.CH_3OH), indicate differences in chemistry and excitation conditions.

The lines of HNCO and $HOCO^+$ highlight the north cloud, and are tracers of shock chemistry.

The lines of SO and SO_2 are also tracers of shocks, and are concentrated at Sgr B2(M), although the lower excitation 99.30-GHz SO line also traces the more extended gas in the north cloud and ridge to the west.

5 SUMMARY

We have undertaken a 3-mm spectral-line imaging survey of the Sgr B2 area, of 5×5 arcmin^2, with the Mopra telescope, at resolution ~ 36 arcsec. We covered almost the complete spectral range 81.7–113.5 GHz, with 2.2 MHz or $\sim$6 km s^{-1} spectral channels, and have observed 24 lines, with 0.033 MHz, or $\sim$0.1 km s^{-1} channels. We have discussed the distribution of around 50 lines, and presented integrated emission images for 38 of the lines. In addition, we have detected around 120 more lines, mostly concentrated at Sgr B2(N).

By fitting the peak position and velocity of the emission in the various lines, we find that there are seven distinct molecular features in the region, which show distinct differences in both molecular abundances and excitation conditions.

ACKNOWLEDGMENTS

The Mopra telescope is funded by the Commonwealth of Australia as a National Facility managed by CSIRO as part of the Australia Telescope. The UNSW MOPS digital filter bank was provided with funding from the Australian Research Council, University of New South Wales, Sydney University, Macquarie University and the CSIRO ATNF. PAJ thanks the Max-Planck-Institut für Radioastronomie, Bonn, for a Visiting Fellowship in 2006, and the anonymous referee for comments that improved the presentation of the paper.

REFERENCES

Bains I. et al., 2006, MNRAS, 367, 1609
Belloche A., Comito C., Hieret C., Menten K. M., Schilke P., Müller H. S. P., 2005, in Lis D.C., Blake G.A., Herst E., eds, Proc. IAU Symp. 231, Astrochemistry: Recent Successes and Current Challenges. Cambridge Univ. Press, Cambridge, p. 332 P
Belloche A., Comito C., Hieret C., Menten K. M., Müller H. S. P., Schilke P., 2007, in Lemaire J. L., Combes F., eds, Molecules in Space & Laboratory. S. Diana, Paris, p. 10
Caswell J. L., 1996, MNRAS, 283, 606
Chung H. S., Ohishi M., Morimoto M., 1994, J. Korean Astron. Soc., 27, 1
Churchwell E., Hollis J. M., 1983, ApJ, 272, 591
Comito C., Schilke P., Phillips T. G., Lis D. C., Motte F., Mehringer D., 2005, ApJS, 156, 127
Cragg D. M., Johns K. P., Godfrey P. D., Brown R. D., 1992, MNRAS, 259, 203
Cummins S. E., Linke R. A., Thaddeus P., 1986, ApJS, 60, 819
de Vicente P., Martin-Pintado J., Wilson T. L., 1997, A&A, 320, 957
de Vicente P., Martín-Pintado J., Neri R., Colom P., 2000, A&A, 361, 1058
Eisenhauer F., Schödel R., Genzel R., Ott T., Tecza M., Abuter R., Eckart A., Alexander T., 2003, ApJ, 597, L121
Garwood R. W., 2000, in Manset N., Veillet C., Crabtree D., eds, ASP Conf. Ser. Vol. 216, Astronomical Data Analysis Software and Systems IX. Astron. Soc. Pac., San Francisco, p. 243
Gaume R. A., Claussen M. J., 1990, ApJ, 351, 538
Gaume R. A., Claussen M. J., de Pree C. G., Goss W. M., Mehringer D. M., 1995, ApJ, 449, 663
Gerin M., Combes F., Encrenaz P., Linke R., Destombes J. L., Demuynck C., 1984, A&A, 136, L17
Goldsmith P. F., Snell R. L., Hasegawa T., Ukita N., 1987, ApJ, 314, 525
Goldsmith P. F., Lis D. C., Lester D. F., Harvey P. M., 1992, ApJ, 389, 338
Gordon M. A., Berkermann U., Mezger P. G., Zylka R., Haslam C. G. T., Kreysa E., Sievers A., Lemke R., 1993, A&A, 280, 208
Greaves J. S., Nyman L.-A., 1996, A&A, 305, 950
Greaves J. S., Williams P. G., 1994, A&A, 290, 259
Hasegawa T., Sato F., Whiteoak J. B., Miyawaki R., 1994, ApJ, 429, L77
Hasegawa T., Arai T., Yamaguchi N., Sato F., 2008, Ap&SS, 313, 91
Hieret C., Belloche A., Comito C., Menten K. M., Schilke P., 2005, in Lis D.C., Blake G.A., Herst E., eds, Proc. IAU Symp. 231, Astrochemistry: Recent Successes and Current Challenges. Cambridge Univ. Press, Cambridge, p. 67P
Hoffmann W. F., Frederick C. L., Emery R. J., 1971, ApJ, 164, L23
Hunt M. R., Whiteoak J. B., Cragg D. M., White G. L., Jones P. A., 1999, MNRAS, 302, 1
Jacq T., Baudry A., Walmsley C. M., Caselli P., 1999, A&A, 347, 957
Kuan Y.-J., Snyder L. E., 1996, ApJ, 470, 981
Ladd N., Purcell C., Wong T., Robertson S., 2005, Publ. Astron. Soc. Aust., 22, 62
Lequeux J., 1962, Ann. d'Astrophysique, 25, 221
Leurini S., Schilke P., Menten K. M., Flower D. R., Pottage J. T., Xu L.-H., 2004, A&A, 422, 573
Leurini S., Schilke P., Wyrowski F., Menten K., 2005, in Lis D.C., Blake G.A., Herst E., eds, Proc. IAU Symp. 231, Astrochemistry: Recent Successes and Current Challenges. Cambridge Univ. Press, Cambridge, p. 99 P
Lis D. C., Goldsmith P. F., 1989, ApJ, 337, 704
Lis D. C., Goldsmith P. F., 1990, ApJ, 356, 195
Lis D. C., Goldsmith P. F., 1991, ApJ, 369, 157
Liu S.-Y., Mehringer D. M., Miao Y., Snyder L. E., 1998, ApJ, 501, 680
Lovas F. J., 2002, J. Phys. Chem. Ref. Data, 21, 181 http://physics.nist.gov/PhysRefData/Micro/Html/
Martin-Pintado J., de Vicente P., Fuente A., Planesas P., 1997, ApJ, 482, L45
McGrath E. J., Goss W. M., De Pree C. G., 2004, ApJS, 155, 577
Mehringer D. M., 1995, ApJ, 454, 782
Mehringer D. M., Menten K. M., 1997, ApJ, 474, 346
Mehringer D. M., Palmer P., Goss W. M., Yusef-Zadeh F., 1993, ApJ, 412, 684
Mehringer D. M., Goss W. M., Palmer P., 1994, ApJ, 434, 237
Miao Y., Mehringer D. M., Kuan Y.-J., Snyder L. E., 1995, ApJ, 445, L59
Minh Y. C., Irvine W. M., Ziurys L. M., 1988, ApJ, 334, 175
Minh Y. C., Haikala L., Hjalmarson A., Irvine W. M., 1998, ApJ, 498, 261
Nummelin A., Bergman P., Hjalmarson A., Friberg P., Irvine W. M., Millar T. J., Ohishi M., Saito S., 1998, ApJS, 117, 427
Nummelin A., Bergman P., Hjalmarson Å., Friberg P., Irvine W. M., Millar T. J., Ohishi M., Saito S., 2000, ApJS, 128, 213
Ohishi M., Ishikawa S.-I., Amano T., Oka H., Irvine W. M., Dickens J. E., Ziurys L. M., Apponi A. J., 1996, ApJ, 471, L61
Oka T., Hasegawa T., Sato F., Tsuboi M., Miyazaki A., 1998, ApJS, 118, 455
Palmer P., Goss W. M., 1996, Galactic Cent. Newsletter, 2, 3
Piddington J. H., Minnett H. C., 1951, Australian J. Sci. Res., 4, 459
Pierce-Price D. et al., 2000, ApJ, 545, L121
Price S. D., Egan M. P., Carey S. J., Mizuno D. R., Kuchar T. A., 2001, AJ, 121, 2819
Reid M. J., 1993, ARA&A, 31, 345
Reid M. J., Schneps M. H., Moran J. M., Gwinn C. R., Genzel R., Downes D., Roennaeng B., 1988, ApJ, 330, 809
Requena-Torres M. A., Martín-Pintado J., Rodríguez-Franco A., Martín S., Rodríguez-Fernández N. J., de Vicente P., 2006, A&A, 455, 971
Sato F., Hasegawa T., Whiteoak J. B., Miyawaki R., 2000, ApJ, 535, 857
Sawada T., Hasegawa T., Handa T., Cohen R. J., 2004, MNRAS, 349, 1167
Snyder L. E., Kuan Y.-J., Miao Y., 1994, in Wilson T. L., Johnston K. J.,

eds, The Structure and Content of Molecular Clouds. Springer-Verlag, Berlin, p. 187
Tsuboi M., Handa T., Ukita N., 1999, ApJS, 120, 1
Turner B. E., 1989, ApJS, 70, 539
Vrtilek J. M., Gottlieb C. A., Thaddeus P., 1987, ApJ, 314, 716
Wilson T. L., Snyder L. E., Comoretto G., Jewell P. R., Henkel C., 1996, A&A, 314, 909
Yusef-Zadeh F., Uchida K. I., Mehringer D. M., Roberts D., Nyman L.-A., Casement S., Lindqvist M., 1996, in Gredel R., ed., ASP Conf. Ser. Vol. 102, The Galactic Center. Astron. Soc. Pac., San Franciso, p. 60

This paper has been typeset from a TEX/LATEX file prepared by the author.